**Title:** Experimental Quality Control Induces Changes in Allen Mouse Brain Connectomes

**Authors/Affiliations:** Vikram Nathan*[1,2,a], Stephanie Tullo[1,b], Lizette Herrera-Portillo[1,2,c], Gabriel A. Devenyi[1,3,d], Yohan Yee[4,5,e], M. Mallar Chakravarty*[1,3,6,f]

[1]Cerebral Imaging Center, Douglas Mental Health University Institute, Montréal, QC, Canada
[2]Integrated Program in Neuroscience, McGill University, Montréal, QC, Canada
[3]Department of Psychiatry, McGill University, Montréal, Canada
[4]Department of Radiology, Cumming School of Medicine, University of Calgary, Calgary, AB
[5]Experimental Imaging Centre, Cumming School of Medicine, University of Calgary, Calgary, AB
[6]Department of Biological & Biomedical Engineering, McGill University, Montréal, Canada
* *denotes corresponding authors*

Emails: [a]vikram.nathan@mail.mcgill.ca, [b]stephanie.tullo94@gmail.com; [c]liz1296@hotmail.com; [d]gdevenyi@gmail.com, [e]yohan.yee@ucalgary.ca, [f]mallar.chak@gmail.com

**Abstract**

The Allen Mouse Brain Connectivity Atlas (AMBCA) is widely used to represent structural connectivity in the mouse brain. The AMBCA consists of tracer injection experiments where neuronal projections axonally connected to the initial injection site are labelled. The resulting whole-brain structural connectomes, derived from a subset of these experiments in C57BL/6 mice, have been used in several studies of connectomic architectures. However, through close inspection of n=437 distinct experiments used in a publicly-available connectome (Knox et al., 2018), we observed experiments with off-target injections, diffuse projections, unrealistically small injections and projections, and anatomical misalignments, affecting the accuracy and applicability of these connectivity experiments. We applied a combined automated and manual quality control (QC) and identified n=56 (~13% of the original n=437) experiments representing a wide variety of injection and projection failures across the brain. Automated QC was used to detect extreme injection and projection sizes and misalignments, while manual QC was used to detect subtle off-target tracer spreading. Using the remaining n=375 experiments, we rebuilt two different connectomes using previously-published methods; specifically: the regionalized voxel model from Knox et al. (2018), and the homogeneous model from Oh et al. (2014). Our rebuilt connectomes show strong losses in connectivity between regions with limited evidence of structural connectivity by other methods (e.g. hippocampus-medulla, cerebellum-isocortex) and gains in connectivity between regions with strong connectivity evidence (hypothalamus-cerebellum, hypothalamus-isocortex). Finally, we analyzed the rich club and community organization to demonstrate the potential downstream impacts on the representation of the overall structural connectome architectures of our QC'd connectomes and observed subtle whole-brain organizational changes. We present our rebuilt connectomes, and particularly highlight the regionalized voxel model, as more accurate representations of structural connectivity derived from the AMBCA.

## Introduction

The Allen Mouse Brain Connectivity Atlas (AMBCA) is often used as the gold standard for mouse brain structural connectivity (Oh et al., 2014). In addition to diverse transgenic lines to visualize cell types of interest, the AMBCA consists of serial two-photon microscopy experiments in ~500 wild-type (WT) adult, male C57BL/6J mice (postnatal days P56 ± 2). Each "experiment" refers to an anatomically distinct injection of a recombinant adeno-associated viral (rAAV) tracer, which expresses enhanced green fluorescent protein (EGFP) under the control of a human synapsin I promoter to specifically label neurons. The tracer spreads anterogradely from the injection site and cannot cross synapses, allowing for the *ex vivo* imaging of the directed, monosynaptic neuronal projections connected to the injection site. The resulting images from these experiments have been used to reconstruct whole-brain axonal connectomes at the regional and voxel levels (Oh et al., 2014; Knox et al., 2018 respectively) that provide significant advantages over commonly used diffusion weighted imaging data acquired using magnetic resonance imaging (MRI): the measured connectivity is direct, rather than probabilistic; all connections are unidirectional and monosynaptic, and the high-resolution of the serial microscopy experiments (0.35 μm) allows for the explicit representation of crossing fibers (Behrens and Sporns, 2012).

These structural connectomes are widely used to interrogate the network architecture of the whole mouse brain. Recent voxel-level anatomical insights include the characterization of hierarchical cortico-thalamic connectivity, an interconnected community recapitulating the default-mode functional network, and differential projections from the thalamic innervations of distinct cerebellar nuclei (Harris et al., 2019; Coletta et al., 2020; Kebschull et al., 2020). These connectomes have also been used to multimodally assess the relationship between monosynaptic connectivity, structural covariance between the thalamus and cortex, and gene expression (Yee et al. 2024; Yee et al., 2018). Because of its anatomical specificity and spatial coverage, the AMBCA has also been used to model whole-brain pathophysiology across a range of pathologies (Mezias et al., 2017; Mezias et al., 2020; Cornblath et al., 2021; Zhou et al., 2025; Torok et al., 2025). A prime example is neurodegenerative disease modelling using the regional connectome from Oh et al. (2014) to simulate the network spreading of pathogenic agents in neurodegenerative diseases, including alpha synucleinopathies and tauopathies, providing mechanistic insights into progressive pathological spreading (Tullo et al., 2025; Rahayel et al., 2022; Henderson et al., 2019; Lubben et al., 2024; Ramirez et al., 2023). In analogous models of pathological spreading in humans, simulations using different connectomic architectures show that modality-specific false positives and negatives can dramatically alter model predictions (Thompson et al., 2024). Therefore, it is critical to have accurate representations of the underlying connectome to understand models of brain organization in the context of brain function and dysfunction.

There are two different connectome models derived from the AMBCA that are commonly used and publicly available: the regional connectome ("homogeneous model", HM) in Oh et al. (2014), and the voxel-level connectome ("voxel model") in Knox et al (2018). The HM takes the injection volume from each experiment and assigns the projection to the injected region(s) based on the size of the injection within each region, regardless of the injected location within the region. The voxel model assigns the projection volume to the centroid of the injected region, while inferring connectivity to neighboring voxels using a distance-weighted average.

However, while examining the potential use of these connectomes for other projects in our group, we observed experiments with off-target injections, diffuse projections, unrealistically small injections and projections, and anatomical misalignments, in spite of the quality control (QC) procedures documented in their respective publications (Figure 1). These failures may result in the over- or under-representation of connectivity to the injected region.

To address this confound, we applied a detailed QC procedure to the n=437 experiments that survived QC in Knox et al. (2018), as well as an additional n=10 WT experiments that were added to the Allen API after 2018. We then rebuilt the homogeneous (HM) and regionalized voxel-model (RVM) connectomes using the n=382 remaining experiments and characterized the impact of using our QC'd connectome on structural connectivity metrics, including the normalized connection strength and top 20% of connections between brain regions. We also examined the downstream impact on graph theory metrics that are commonly used in the connectomics literature, including the rich club and Louvain communities (Van den Heuvel and Sporns, 2011; Gollo et al., 2015; Swanson et al., 2017; Brooks et al, 2024; Coletta et al., 2020; Herrera-Portillo et al., 2025; Ashourvan et al., 2019). We posit that our rebuilt connectomes represent a cleaner, more accurate map of structural connectivity in the mouse brain.

## Methods

*Methods Overview*

Our analysis was divided into three main phases: automated QC, manual QC, and characterizing rebuilt whole-brain connectomes after excluding the experiments that did not pass our QC standards (Methods figure). All of our QC'd data was aligned to the Allen Institute's Common Coordinate Framework, version 3 (CCFv3) template (Wang et al., 2020). We primarily assessed architectural changes in the voxel model, which assigns the connectivity from each experiment to the centroid of the experiment's injection site, while assuming spatial smoothness for the remaining voxels (Knox et al., 2018). We also characterized the changes in the homogeneous model, which assigns connectivity to parcellated brain regions based on the injection size, regardless of the location of injection within a given brain region (Oh et al., 2014). Finally, we applied graph theoretical metrics to the old vs. new Knox connectome to assess whole-brain organizational changes upon rebuilding the connectome.

---

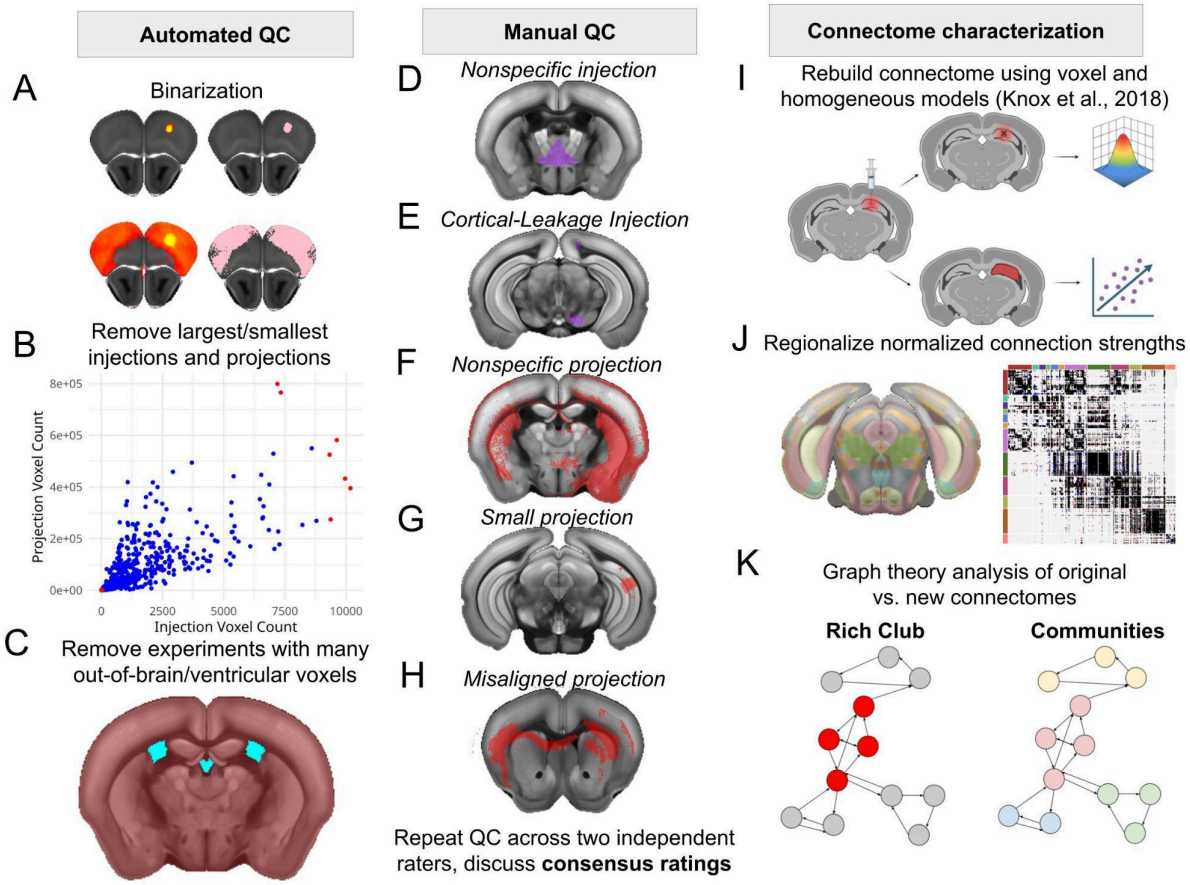


**Figure 1: Methods overview**. Our workflow consists of three main phases. 1: Automated QC, including (A) binarization using injection and projection-specific thresholds of 0.5 and 0.1 (B) using robust outlier filtering to remove the largest injections and projections, and identifying the smallest four injections and projections (C) removing experiments with the largest and smallest counts of out-of-brain or ventricular voxels, using robust outlier filtering removing experiments with manual QC, and assessment of downstream impacts on the rebuilt structural connectomes. 2: Manual QC for injections, including (D) nonspecific injections and (E) cortical-leaking injections; manual QC for projections, including (F) nonspecific/widespread, (G) small, and (H) misaligned projection densities. 3: Connectome characterization, including (I) rebuilding the RVM and HM (J) regionalizing the normalized connection strength metric, and (K) rich club and community analyses on the top 20% of connections in the original vs. rebuilt connectomes.

---

*Defining Injection Density and Projection Density*

To define neuronal connectivity to a variety of regions across the whole-brain, the original authors at the Allen Institute conducted n=491 experiments in C57BL/6 mice using a fluorescent, adeno-associated virus (AAV) tracer that specifically entered the soma of infected neurons. 21 days following each injection, mice were euthanized and their brains were extracted for serial two-photon microscopy, resulting in a series of 2D images, which were segmented by the Allen Institute to define injection masks and projection data (see *Experimental and 2D Image Processing for Serial Two-Photon Microscopy Data* in Supplementary Methods for more

details). These images were then stacked to form 3D injection and projection images. The stacked 3D images were then aligned to the Allen Institute's 3D reference model, the Common Coordinate Framework (Version 3, "CCFv3"), using linear and nonlinear registration.

The aligned 3D injection and projection data (0.35 µm x 0.35 µm x 100 µm) were resampled into isotropic voxels at various resolutions before defining voxel-level metrics; we chose the resampled data at a 50 µm resolution for our analyses, between the finest resolution available (25 µm) and the resolution used to build the connectomes (100 µm). The "injection fraction" was defined as the fraction of 2D pixels in each voxel belonging to the manually annotated injection site, and "injection density" and "projection density" as the sum of segmented injection/projection pixels divided by the sum of all pixels in each voxel. Knox et al. (2018) used the term "injection density" to refer to the product of the aforementioned injection fraction and injection density values, representing the proportion of segmented neurons in the annotated injection area. We apply the same definition of "injection density" as Knox et al. (2018).

We downloaded the injection fraction, injection density, and projection density from the Allen API for all included (n=427) and excluded (n=63) experiments from Knox et al. (2018). Although Knox et al. (2018) reported n=428 included experiments, experimental data was no longer available to download for tracer 310207648, so this experiment was excluded from all subsequent analyses. We also QC'd ten additional WT experiments that were automatically downloaded by the mouse_connectivity_models package when rebuilding all connectomes (see *Rebuilding the Regionalized Voxel and Homogeneous Model Connectomes*), resulting in a total of n=437 QC'd experiments.

*Transforming and Thresholding Injection Density and Projection Density*
After downloading the injection and projection data, we converted data from the PIR (+x: Posterior-Anterior, +y: Inferior-Superior, +z: Right-Left) space used by the Allen institute to RAS (+x: Right-Left, +y: Anterior-Posterior, +z: Superior-Inferior) coordinates. RAS coordinates are the canonical orientation in preclinical imaging and are compatible with our existing image analysis pipelines (Ionas et al., 2021; Desrosiers-Grégoire et al., 2024; Germann et al., 2025). We rotated the axes and redefined the position of the origin to the center of the anterior commissure as it crosses the sagittal midplane, consistent with the standard DSURQE MRI atlas (Dorr et al., 2008; Steadman et al., 2014; Ullmann et al., 2013; Richards et al., 2011; Qiu et al., 2018). For anatomical analyses of the injection and projection data, we downloaded the most recent CCFv3 template (Wang et al., 2020) and label file from the Allen API and repeated the above transformation. Additionally, we created a brain mask from the nonzero values in the label file.

We sought to ensure that any experimental failures were not simply due to the lowest injection and projection values, which could represent poorly segmented projection data or autofluorescence. To this end, our automated and manual QC only considered injection density values over 0.5 and projection density values over 0.1 (Figure 1A), values that were heuristically chosen after visual inspection to retain the majority of the injection and projection data while eliminating noise. These thresholds were similar to the threshold of 0.2 applied to the projection density data within the *Brain Explorer* application used to visualize the Allen Brain Connectivity Atlas (Feng et al., 2015). These binarized files were used for automated QC, and to generate slice

images for manual QC. Note that when rebuilding the connectome, we used the full, unthresholded data (see *Rebuilding the Regionalized Voxel and Homogeneous Models*).

*Automated Quality Control*

Before visually inspecting all experiments, we defined automated exclusion criteria. We defined the "projection" and "injection" voxels for each experiment from its binarized projection density (0.1 threshold) and binarized injection density (0.5 threshold), respectively (Figure 1A). We first excluded experiments with the largest numbers of out-of-brain and ventricular projection voxels, using the CCFv3 brain mask and ventricular region labels in the CCFv3 label file to identify failed experiments (Figure 1B). These failed experiments represent alignment failures when stacking or registering the 2D microscopy data to the 3D template, particularly evident with corpus callosum misalignment, or experimental failures with the tracer spreading nonspecifically throughout the brain (Figure 1F). For our ventricle analysis, we did not consider voxels in the third ventricle and cerebral aqueduct, as these regions were too thin to robustly capture misaligned experiments. We then examined the distributions of the number of out-of-brain and ventricular projection voxels, identifying outliers using exponential right skewness adjustment coefficients multiplied by the values 1.5 times the interquartile range (IQR) from the median. For more information, see formula 5 in Hubert and Vandervieren (2008), which was implemented in the *robustbase* package in R (Hubert and Vandervieren, 2008; Maechler et al., 2025).

We excluded experiments with the largest and smallest injection and projection voxel counts (Figure 1C; see Figure 2B, results), viewing these extrema as experimental failures and biologically implausible connections. For upper outliers, we discarded experiments with injection or projection voxel counts that met the same right-skewness-adjusted robust outlier filtering criteria as for the out-of-brain and ventricular voxel counts. For lower outliers, we excluded experiments with the bottom four smallest injection and projection voxel counts.

*Manual Quality Control*

We manually QC'd all n=437 experiments' injection and projection densities to detect nuanced experimental failures. For example, an implausibly small projection from a well-connected brain region like the hippocampus would still be larger than a biologically realistic cerebellar projection; hence, "small" vs. "nonspecific" injection and projection volumes depend on the region of injection. For standardized inspection, we generated ten equidistant slice images along each dimension, overlaid atop the CCFv3 template. We then QC'd all images using PyQC (see https://github.com/CoBrALab/ for make_slice_images and PyQC ). For injection or projection volumes with no voxels on the chosen slices, we generated cropped slice images based on the location of the injection or projection. For full QC images, see Supplementary Data 1.

We then applied separate QC criteria to the injection and projection images. For all images, we defined a rating of "0" as a "pass," and a rating of "4" as a partial failure not severe enough for removal. For the injection images, a rating of "1" (Figure 1D) denotes a large or nonspecific injection spanning multiple brain regions. A rating of "2" (Figure 1E) denotes subcortical injections with substantial cortical leakage, or, conversely, a cortical injection that also infects subcortical areas, generalizing the criteria from Knox et al. (2018). For the projection images, "1" (Figure 1F) denotes nonspecific tracer spreading to off-target regions spanning multiple major brain divisions, "2" (Figure 1G) denotes little or no long-distance projections from the

injection site (outlined in Knox et al.), and “3” (Figure 1H) denotes a misalignment to the anatomical template. We removed all experiments that met these criteria before rebuilding the RVM and HM connectomes (see Supplementary Data 2 for full list of all numerical ratings).

Note that we also defined a rating of “5” for a projection experiment with a very small number of out-of-brain voxels that is not necessarily misaligned, and a rating of “9” for an experiment with no injection or projection data in the original ten-slice QC image, prompting further investigation into the cropped image. The "9" images did not necessarily have the smallest number of projection voxels, but often had voxels between the default slices generated by PyQC. The “5” images mainly appeared at the lower binarization thresholds (0.01) and had within-brain voxels that aligned well with the anatomy of the underlying template, indicating possible partial-volume effects that could be masked out, rather than a registration failure. Hence, we chose to keep experiments that met these criteria.

Two independent raters (V.N, S.T.) evaluated all injection images at a 0.5 binarization threshold and projection images at a 0.1 threshold before meeting to discuss consensus ratings on any disagreements. The final consensus QC ratings for all injection and projection images were used to define which experiments to exclude from further analysis. Additionally, V.N. separately examined manual QC images at a 0.01 threshold to confirm that the designation of “failed” experiments was not threshold-dependent. For the initial disagreements and full ratings for all experiments, see Supplementary Data 2.

*Rebuilding the Regionalized Voxel and Homogeneous Model Connectomes*
After removing experiments that did not pass our QC criteria, we characterized the impact of these removals on canonical models of whole-brain connectivity. The main connectome evaluated was the voxel-level connectome from Knox et al. (2018). This model estimates connectivity by assigning each experiment’s projection strengths to the centroid of the injection site, and infers connectivity to voxels neighbouring the injection site using a spatial kernel. We rebuilt the voxel-level model and summed connection strengths over n=291 gray matter regions to produce the RVM. We then chose the “normalized connection strength” as our output metric, which sums the raw connectivity strength between all voxels in “source” and “target” regions and then divides by the size of the source region.

We also rebuilt the HM connectome from Knox et al. (2018), which is similar to the connectome from Oh et al. (2014) and produces a normalized connection strength by default. This connectome assigns each experiment’s projection strengths to all regions containing the experiment's injection site (“additivity”), and assumes that two equally sized injections within the same source region contribute the same to the fluorescence of the target regions, regardless of their location (“homogeneity”). However, the HM does not exclude any of the n=291 regions, whereas the connectome from Oh et al. (2014) only includes n=213 regions, excluding regions with few injected voxels and regions that are not linearly separable from other regions. Thus, after rebuilding the HM, we only analyzed the n=211 regions that were also in Oh et al. (2014) (specifically excluding the dorsal and ventral subiculum).

To rebuild the RVM and HM connectomes, we reran the algorithms located within the Allen Institute’s *mouse_connectivity_models* package

(https://github.com/AllenInstitute/mouse_connectivity_models), which accessed all n=498 WT experiments in the current version of the Allen API (accessed February 2026) within the *allensdk* package (version 2.16.2, see https://github.com/AllenInstitute/AllenSDK/releases ), but excluded the n=63 experiments originally excluded by Knox et al. (2018). This resulted in a total of n=435 experiments used to rebuild all connectomes before our QC. It is important to note that although we QC'd experiments 100142354 and 112670853 due to their inclusion in the Knox connectome, they were not used for the original or rebuilt RVM or HM connectomes described in this paper.

All parameters remained the same except the list of experiments excluded, resulting in maps of normalized connection strengths. The resulting connectomes contain continuous, positive values of normalized connection strength between any two brain regions.

*Rich Club and Community Detection Analysis*

Finally, we provided examples of how our QC impacts graph theoretical metrics of network-level organization. We examined the top 20% of overall connections across the RVM. Whichever connections remained were then assigned as "edges" to the corresponding source and target regions, which were the "nodes" in our network. We chose two metrics: the topological rich club nodes (based on the continuous rich club coefficient for each node) and the Louvain community assignments for each node. These metrics complementarily capture which nodes are well-connected among themselves and to the rest of the network (rich club), and which groupings of nodes are well-connected between themselves (communities) (see schematic in Figure 1). For all analyses, we used the Brain Connectivity Toolbox (version 2019-03-03) in MATLAB (version R2024b) (Rubinov et al., 2009). Our approach was inspired by similar work that characterized these metrics using the voxel-level connectome in Knox et al. (Herrera-Portillo et al., 2025; Coletta et al., 2020); for algorithmic details, see *Rich Club Algorithm* and *Community Detection Algorithm* in Supplementary Methods.

## Results

*Automated QC Reveals Registration and Experimental Failures*

We identified several experiments as outliers for the number of projection voxels outside the brain (n=3), but no experiments as outliers for ventricular voxels. We note that one of these outliers, experiment 112670863, was included in the original RVM connectome but was no longer available through the *allensdk* package. Further inspection of the projection patterns of the top 'out-of-brain' experiments revealed misalignments to the underlying anatomical template and key visual landmarks like the corpus callosum (Figure 2A). Despite not being identified as outliers after skewness adjustments, the top two experiments for ventricular voxels were identified as outliers for the largest overall projection volumes, indicating that the number of ventricular voxels could capture diffuse, non-specific tracer spreading (Figure 2A, 2B).

We also identified upper and lower extrema for injection and projection voxel sizes (Fig. 2B and 2C, respectively) and compared the binarized injection and projection voxel counts to experiments that failed the QC criteria in Knox et al. (2018). Importantly, we see that our identified outliers for the largest projections, largest injections, and smallest injections are more extreme than those identified in Knox et al. (2018), and that our excluded experiments for smallest projections are within 100 voxels of those excluded by Knox et al. (2018) (Fig. 2C).

In total, after these automated QC steps, we removed n=17 experiments (Supplementary Figure 1). However, we also observed that the experiments removed by Knox et al. (2018) show a diverse range of injection and projection voxel counts, indicating more nuanced experimental failures that were specific to the injected region (Fig. 2B). Thus, manual QC was necessary for us to assess the remainder of our failure modes (Figure 1).

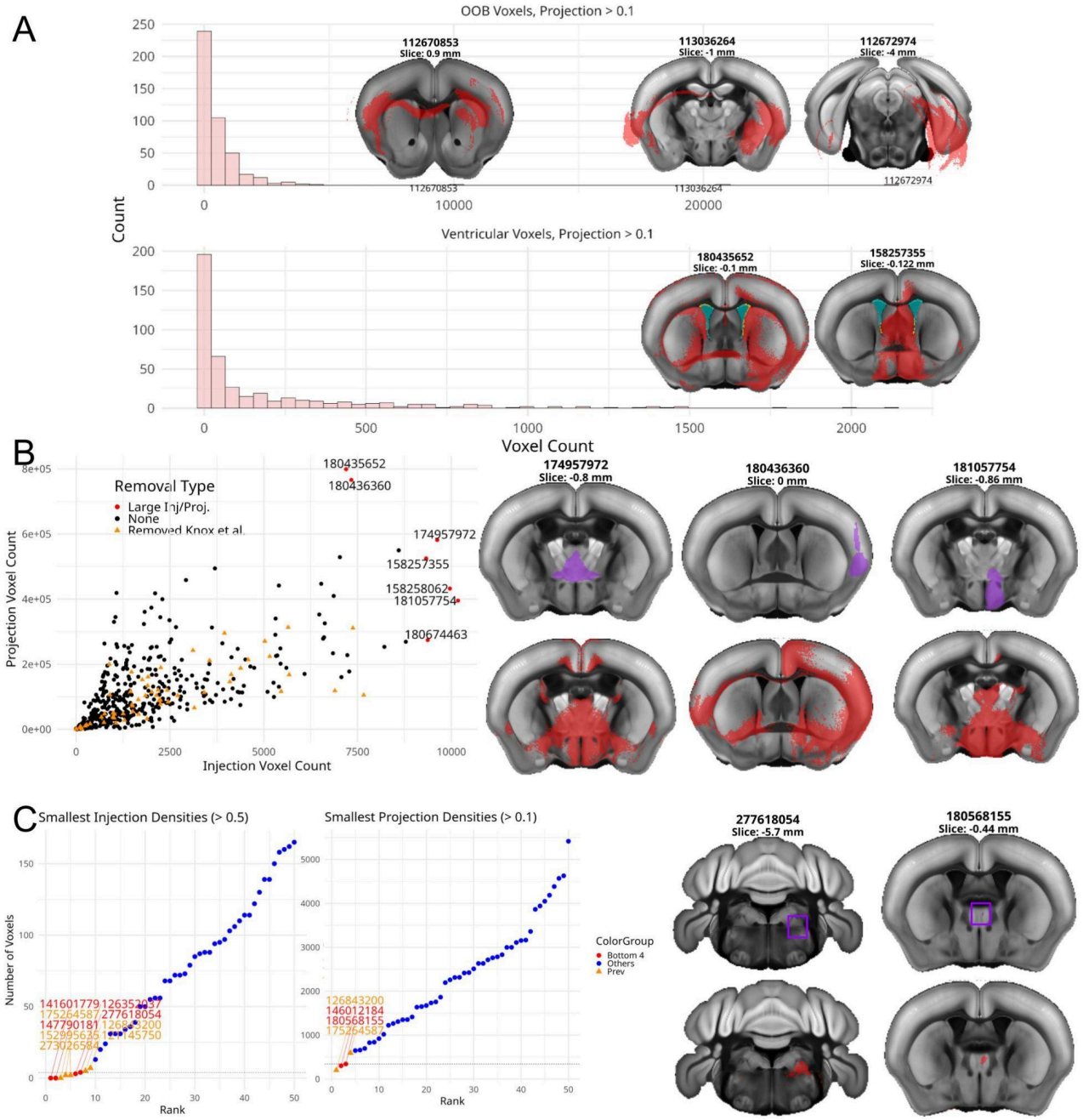


**Figure 2:** Automated QC results identify many experimental failures, including: (A) experiments that are significant outliers for out-of-brain voxel counts (after robust outlier filtering), and severe experiments for the number of ventricular voxels, indicating misalignment and/or nonspecific tracer spreading (B) experiments that contain the highest number of injection and projection voxel points, overrepresenting connectivity to injected regions and biasing the connectome with nonspecific tracer spreading and (C) experiments with the lowest number of injection and projection voxel counts, underrepresenting connectivity to a given region. Note that all counts are calculated on the thresholded, binarized data.

*Manual QC Reveals Spatially and Qualitatively Diverse Failures*
Two independent raters applied our manual injection and projection QC criteria to all n=437 experiments prior to deciding on consensus ratings (see *Methods*). We observe a high inter-rater reliability in the injection QC criteria (86%) and projection QC criteria (86%) before consensus adjustment. Our consensus ratings resulted in the manual removal of n=50 experiments. Of these experiments, n=11 were already excluded by automated QC, resulting in a total of n=56 excluded experiments across all failure types (Supplementary Figure 1).

We observe a wide variety of experiments removed across major brain divisions and failure modalities (Figure 3C), with the greatest number of removed experiments with injections in the hypothalamus, hippocampus, and midbrain. When examining the first failure mode for each experiment, we also noticed consistencies across major brain divisions. For example, all n=3 failed cerebellar experiments had small projections. Additionally, for the n=18 failed hypothalamic and midbrain experiments, all but two of the experiments had off-target injections. Nonetheless, for the hippocampal formation, we also observed a mix of connectivity failures, including out-of-brain projections (n=1), cortical leaking injections (n=3), small projections (n=5), and misaligned projections (n=1).

To examine the locations of the lost connectivity, we calculated the number of removed injections (thresholded and binarized) per Allen brain region and the number of removed projections per voxel (Supplementary Figure 2). We then divided this number by the initial counts of injections within each brain region and projections in each voxel to get the ratio of injection experiments removed per region and projection experiments removed per voxel (Figure 3B and 3C). We chose to examine injection removals per region instead of per voxel due to the relative sparsity of injection volumes compared to projection volumes, and due to the importance of injections per region in the HM from Oh et al. (2014). We find that we lose all injections into small cerebellar subregions and brainstem nuclei, but that all other regions have at least one remaining injection (Fig. 3B). As expected, we lose 100% of projection voxels outside of the brain and within the medial ventricle, but also lose large proportions (~75%) of projections to hypothalamic areas (Fig. 3C). Still, we see a loss in projection voxels across the brain, indicating that our QC removals are not specific to a single brain region.

Notably, among our manually excluded experiments, we observed that automated QC identified a large number of experiments with “manual nonspecific” (n=4/7) and “manual misaligned” (n=3/4) projection failures (Supplementary Figure 1). Additionally, of the n=11 experiments with both manual and automated QC failures, n=3 of these experiments failed at least three independent QC criteria (experiment IDs 158257355, 113036264, and 174957972), providing compelling evidence for removal of these experiments and the validity of our criteria. The most extreme example of this was thalamic injection experiment number 174957972, which was automatically flagged for large injection and large projection, as well as manually flagged for large injection and projection volumes.

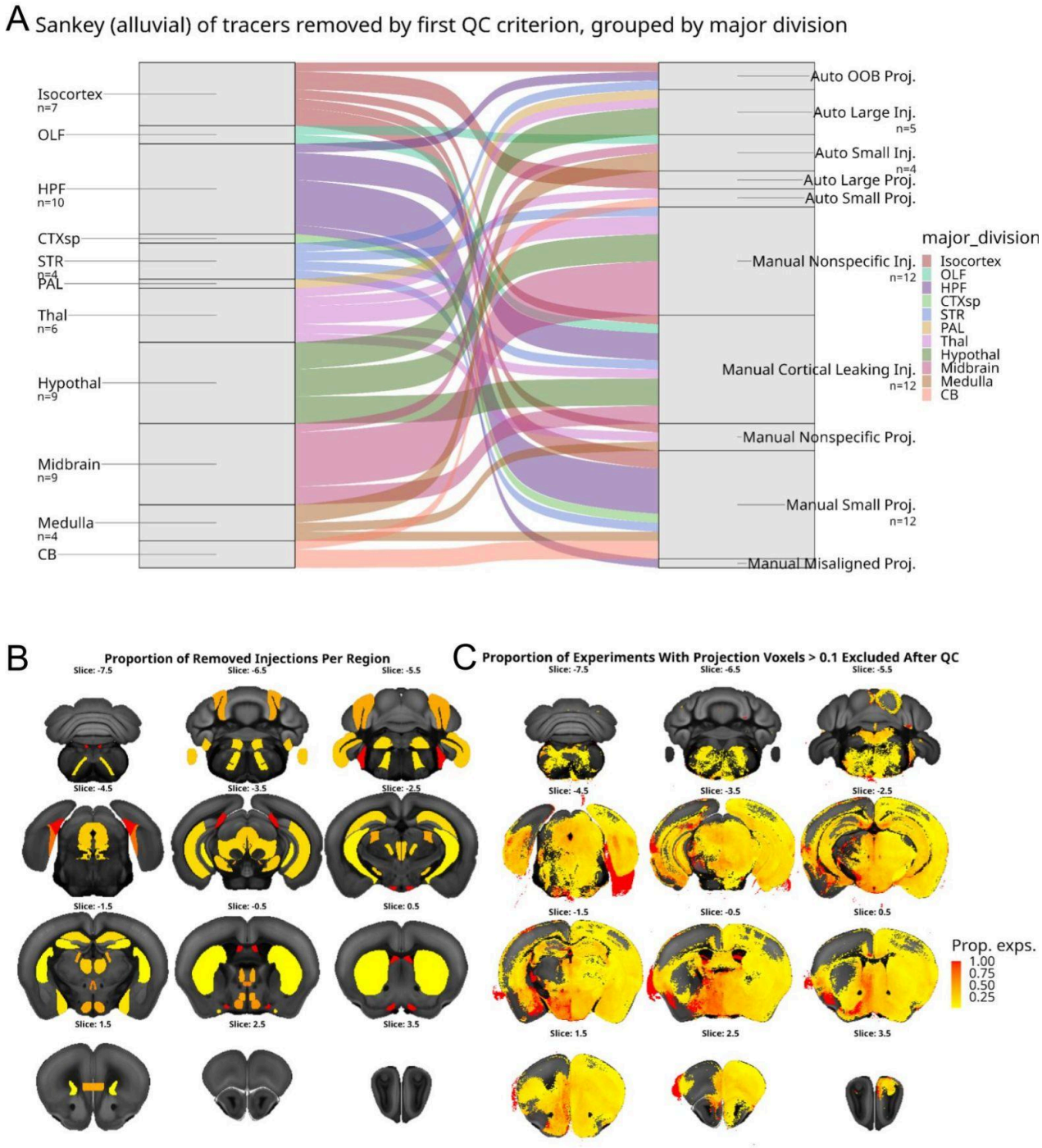


**Figure 3:** We show the full set of manual/automated QC Removals. (A) All excluded experiments are organized by the first exclusion criteria (see Supplementary Figure 1) and the major division injected (abbreviations in Supplementary Table 1), with the number of experiments labelled for categories with greater than three experiments. (B) The proportion of removed injections in each region of the CCFv3 atlas, relative to the total number of experiments that injected each region. (C) The proportion of removed projections in each voxel, relative to the total number of projections in each voxel. The total number of injections/projections in each region/voxel are calculated over all n=437 experiments.

*Continuous Architectural Changes in Rebuilt Connectomes*
After removing the n=56 experiments, we rebuilt the connectivity strengths between n=291 regions in the RVM and n=211 regions in the HM connectome (see *Methods*) (Knox et al. 2018; Oh et al., 2014). We observed minimal changes in the distribution of logged connectivity strengths in the RVM and the HM, relative to the maximum connectivity strength (Supplementary Figure 3).

We then z-scored the "normalized connection strength" in the original vs. rebuilt connectomes, before calculating the difference in z-scored connectivity in the new minus the old RVM and HM connectomes. This procedure reveals strong gains and losses in the z-scored connection strengths between regions in the RVM and HM connectomes following QC (Figure 4A and Supplemental Figure 4A, respectively). Consistent with the distributional changes, we see that the HM shows stronger losses (negative differences) in connectivity, whereas the RVM connectome is more robust to the removed experiments; hence, our main results will focus on the RVM connectome. In the RVM connectome, we observed that the largest losses in z-scored connectivity strength were in hypothalamus-hypothalamus connections (Figure 4A, #1), particularly contralaterally. We also observed strong losses in connection strength between medullary regions and contralateral thalamic (#2) and midbrain (#3) regions, and between isocortical regions and the contralateral olfactory bulb (#4), corticular subplate (#5), and striatum (#6). However, especially for hypothalamus-hypothalamus connections, these strong losses in connectivity strength were often accompanied by a strong gain in connectivity to nearby regions (#7).

We thus examined the overall change in regionalized connection percentile aggregated across major brain divisions. We examined the percentile rather than the z-score due to the wide use of percentile-based thresholding to enforce a network with a given density for connectomic analyses (Fornito et al., 2013). In the RVM connectome, we see the strongest losses in the connectivity of the hypothalamus to the contralateral cortical subplate (-9.46%) and the hippocampus to ipsilateral medulla (-7.97%) (Supplementary Figure 5A). Additionally, we observed widespread losses in cerebellum-forebrain connectivity (isocortex, olfactory bulb, hippocampal formation, corticular subplate), but a strong gain in connectivity to hindbrain divisions (pons, medulla). Ipsilaterally, we also observed a general loss of connectivity to the hypothalamus, especially to the cortical subplate (-3.95%). These changes were consistent with the changes in the HM (Supplementary Figure 6A), especially the strong losses in hippocampus-cerebellum (-4.67%) and hypothalamus-cortical subplate connectivity (-1.64%). Nonetheless, each model shows distinct gains in connectivity; namely ipsilateral cerebellum-pons in the voxel model (+2.37%) and ipsilateral midbrain-cortical subplate in the HM (+2.69%).

*Discrete Architectural Changes in Rebuilt, Thresholded Connectomes*
After characterizing continuous connectivity changes across all connections, we wanted to assess the impact of our QC on the strongest connections, as these are more likely to represent true monosynaptic connectivity patterns between brain regions. We binarized our connectomes before and after QC using two separate thresholds that retained the top 20% and top 5% of connection strengths, inspired by the density of remaining connections after applying high versus low

p-value thresholds, as determined by Oh et al. (2014) (Zalesky et al., 2016). We then visualized the changes in the binarized region-region connectomes.

Although the majority of the strongest connections in the RVM and HM connectomes were retained, at a 20% threshold, we observed brain regions with large numbers of lost and gained binary connections within each model (Figure 4B and Supplementary Figure 4B, respectively). Additionally, we observed more subtle losses and gains in connectivity when comparing the top 5% of connections across both models pre and post-QC (Supplementary Figure 7). Most strikingly, in the RVM connectome, we observed a large number of lost connections between a hippocampal region (identified as the *induseum griseum*) and between the medulla and cerebellum (Figure 4B, #1), as well as between the cerebellum and isocortex (#2). We observed similar losses in hippocampal connectivity within the top 5% of connections in the RVM (Supplementary Figure 7A).

When aggregating the top 20% of connections across major divisions, after QC, 100% of previous connections between the hippocampus and ipsilateral medulla were lost (with only a 4% gain in new connections), and 100% of connections between the hippocampus and contralateral medulla are lost (Supplementary Figure 5B). Similarly, all connections from the olfactory bulb to the cerebellum were lost, and most of the connections between the cerebellum and isocortex were lost (94% ipsi; 100% contra). In the HM, we also observed a 100% loss in hippocampus-medulla and 81% loss in cerebellum-isocortex connections (Supplementary Figure 6B). We also observed a complete loss in the top 5% of connections in the RVM between the hippocampus and medulla (Supplementary Figure 8A).

Conversely, in the RVM connectome, we also observed a 600% gain in the top 20% of connections between the midbrain and ipsilateral cerebellum, a trend that is mirrored by a 55% gain and 5% loss in existing connections in the HM (Supplementary Figure 5B, 6B). Similarly, when examining the larger set of connections between the hypothalamus and contralateral isocortex, we observed a 76% gain in the RVM and a 178% gain/6% loss in original connections in the HM. We also observed general gains in hypothalamus-contralateral cerebellum connectivity (250% gain RVM; 100% gain and 22% loss in HM). Nonetheless, these trends were not present in the top 5% of connections in the HM after QC; we instead observed a general increase in connectivity from the hypothalamus to all major divisions except the cerebellum, a trend that is not present in the RVM (Supplementary Figure 7; Supplementary Figure 8).

Taken together with the continuous changes shown in the previous section, we claim that our QC criteria helps remove spurious connections while preserving and adding biologically meaningful connectivity patterns, a trend that is particularly evident when examining the binarized connectomes from the RVM.

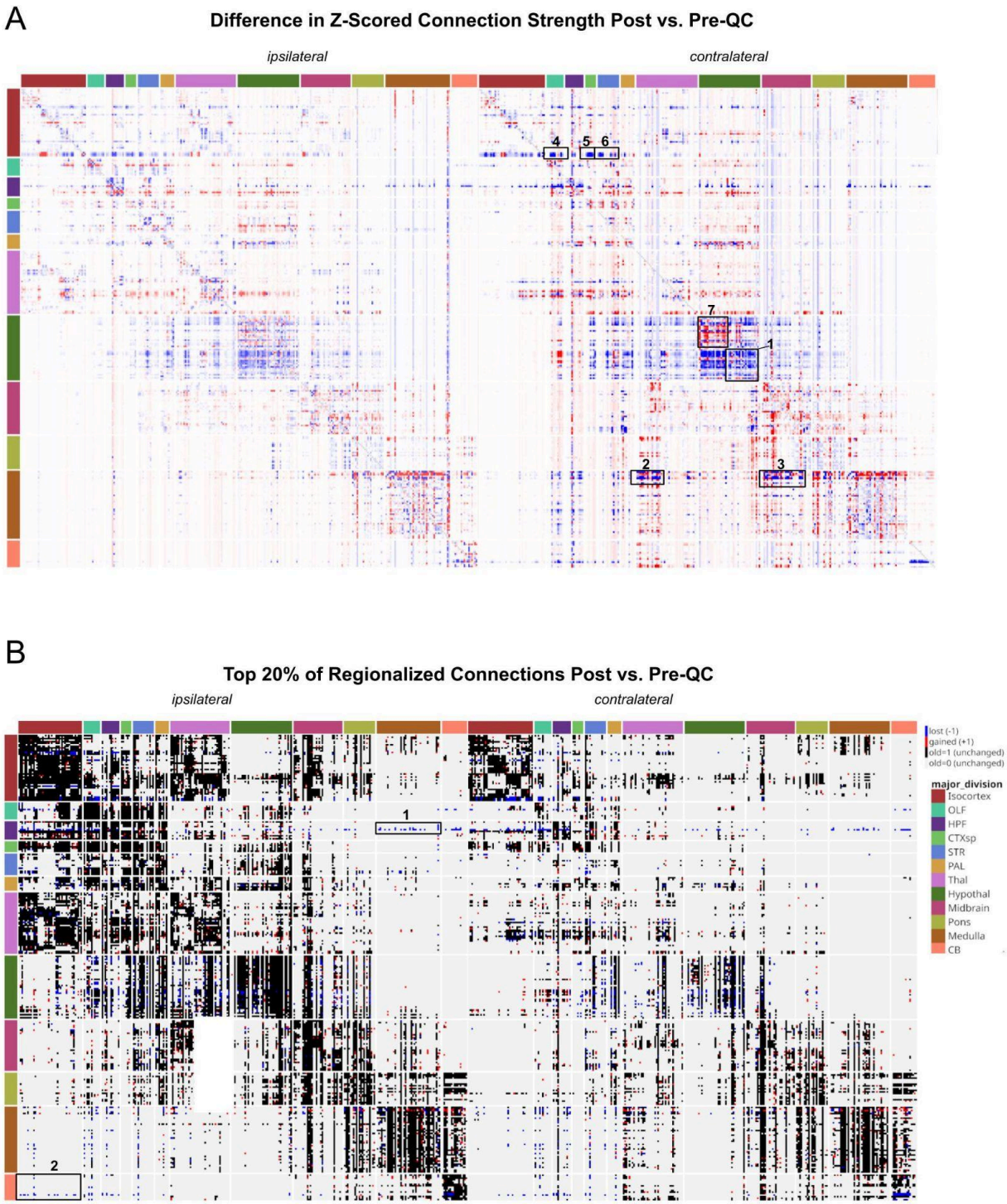


**Figure 4:** We observe whole-brain architectural changes in the RVM (n=291 regions) after QC, when examining the (A) difference in z-scored, normalized connection strengths, thresholded from [-1,1] (B) discretely, when examining the lost (blue), gained (red) and unchanged (black/gray) connections within the subset of the top 20% of the old vs. rebuilt connectomes. The numerical labels correspond to specific gains or losses in connectivity mentioned in the *Results*.

*Graph Theoretical Analysis Reveals Subtle Organizational Changes Following QC*
Following QC, we observed that the rich club coefficients and the topological rich club nodes remain mostly stable (Figure 5A and 5B). We observed the biggest loss in the rich club coefficient for the induseum griseum, a region for which our QC removed spurious connections to the medulla and other hindbrain regions (Figure 5A). We also observed that all ten nodes with the largest changes in rich club coefficient show a loss in the coefficient, including the induseum griseum of the hippocampus, as well as other hypothalamic, cortical, and striatal regions, including the well-connected caudoputamen. Of the top ten nodes, only one region in the cerebellum, the paramedian lobule, showed a gain in the rich club coefficient, but still remained one of the least-connected regions. Additionally, we observed that all but two topological rich club nodes were preserved after QC (Figure 5B). The preserved regions showed similar distributions within the hippocampus, thalamus, and midbrain as a previous voxel-level analysis of the Knox et al. (2018) connectome (Coletta et al., 2020).

After running the Louvain algorithm, we identified four communities in the old and new connectomes, which roughly correspond to brainstem/hippocampus, midbrain, cerebellum/hindbrain, and cortex/olfactory networks (Figure 5C). We further observed changes in the community assignments for 6 regions. On one hand, the diagonal band nucleus changed from the "brainstem/hippocampus" to the "cortical/olfactory" community, whereas the interanteromedial nucleus and lateral habenula of the thalamus changed from the cortical to the brainstem community. Additionally, the substantia nigra, parasubthalamic nucleus, and preparasubthalamic nucleus changed from the midbrain to the cortex/olfactory community.

To confirm that our graph theoretic results were not significantly biased by the size of the target region, we repeated our rich club and community detection analyses on the "normalized connection density," which divides the normalized connection strength between two regions by the size of the target region. We observed similar rich club regions to before, as well as similarities in the rich club coefficient before and after QC, but with a few rich club regions gained after QC (Supplementary Figure 9A/B). Additionally, we identified the same four communities as before, but with a subtle increase in the number of regions in the midbrain community, which now contained regions that were previously assigned to the CB/hindbrain community. The community assignments using the normalized connection density were also more stable following QC, compared to using the normalized connection strength; the only two regions that changed community assignments were the superior colliculus and the lateral habenula, which changed from the cortex to hindbrain and hindbrain to midbrain communities, respectively (Supplementary Figure 9C). Taken together, these results indicate subtle, metric-dependent organizational changes following QC.

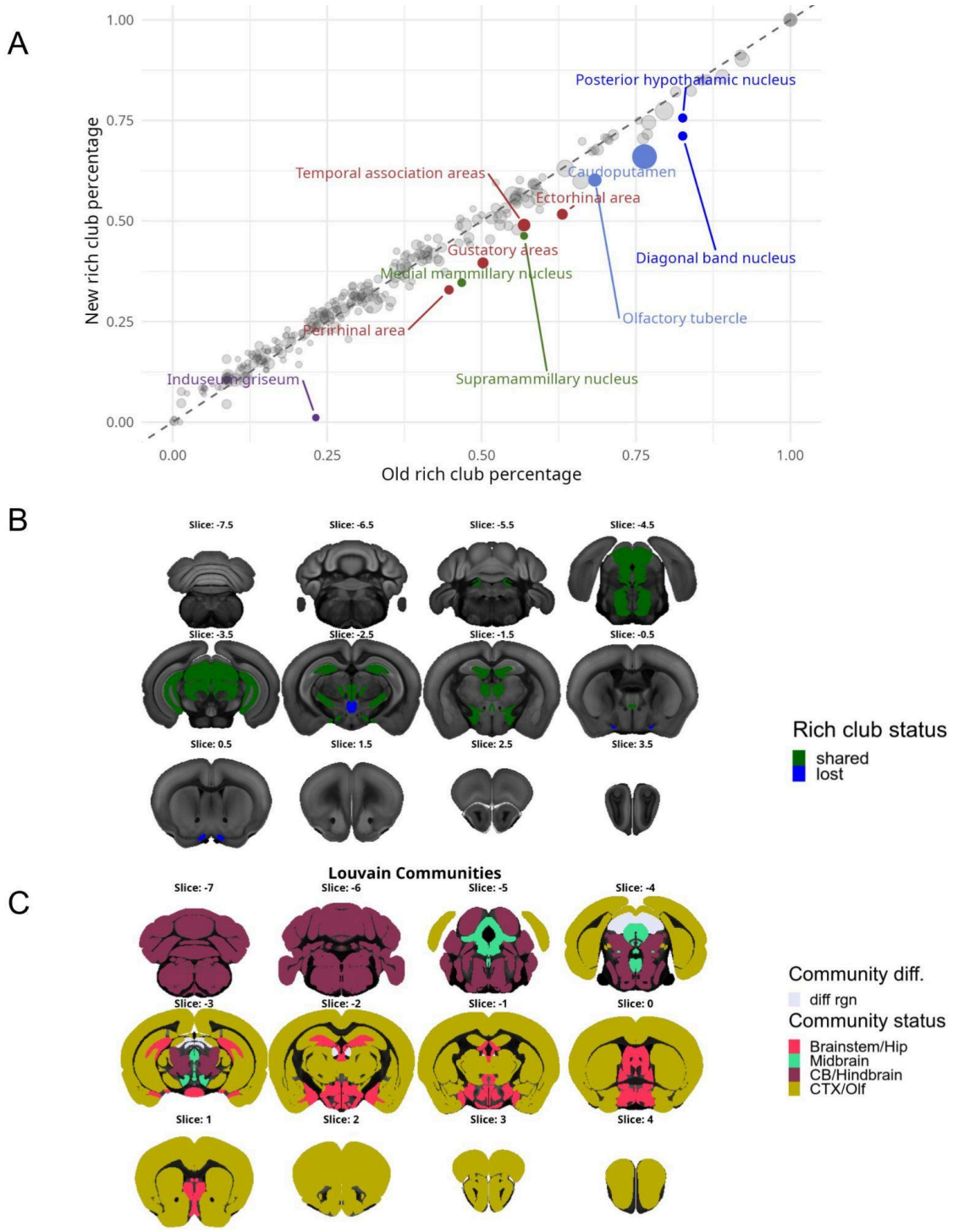


**Figure 5:** Graph theoretical analysis revealed organizational changes within the top 20% of connections in RVM, assuming symmetric connections across hemispheres. We observed changes in (A) the rich club coefficient, defined as the proportion of "rich" degrees that a given region's degree is greater than or equal to (B) whether a region is "rich" or not, using a threshold of the mean plus one standard deviation of the "rich" degrees, and (C) the Louvain community assignments for each region.

**Discussion**

Our quality control procedure identified a set of n=375 experiments that satisfy the credit assignment problem for building whole-brain connectomes; namely, projections were properly aligned and neither too small nor too diffuse to meaningfully represent axonal tracts, and injections were confined to a single brain region. After rebuilding the connectomes on this cleaner subset of the data, we observed large decreases in connection strength percentiles across major divisions. These changes arise from changes in regional-level connectivity, and suggest even stronger changes in voxel-level connectivity, which are particularly relevant to researchers examining specific connections to a single voxel or region of interest.

We excluded n=56 (~13%) of the original 437 experiments, representing a variety of experimental and/or image processing failures. Additionally, of the n=18 experiments removed through our automated QC, n=12 of them were also identified during manual QC, confirming our initial automated filtering step (Supplementary Figure 1). Our automated QC using the brain mask identified three experiments that were grossly misaligned to the CCFv3 template, which could be due to a failure in the registration of the 2D microscopy images to the 3D template. The procedure used for this alignment involved stacking the 2D slices, assuming no missing slices during data collection (Kuan et al., 2015); however, inspecting the data mask for experiment 113036264 reveals missing coronal slices, and these missing slices appeared to not have been padded into the resulting 3D volume. This error resulted in a biologically invalid mask, driving the downstream registration misalignment. We note that, unlike the injection and projection failure modes, re-processing of the misaligned experiments could recover them for future use.

We also observed experiments that are upper and lower extrema for injection and projection voxel counts, or injections that span multiple major brain divisions. We deemed these experiments as biologically unrealistic, and excluded these extreme cases to avoid over or under-representing connectivity to injected brain regions or centroid voxels. The large injections could have arisen from the electrical parameters of the iontophoresis technique used to control the virus' entry into the injection site. The current strength and duration were chosen to produce infection areas of 400 to 700 µm, but it was reported that these parameters would result in larger infections ( >1000 µm) in subcortical areas with lower neuron densities (Harris et al., 2012). These large injections could have also been due to a large or broken pipet tip (Harris et al., 2012). We show that these large injections are highly correlated with larger projection volumes (Figure 2B). On the other hand, our manual and automated QC identify experiments with small injection sites and barely any projections beyond these injection sites, which could have been due to low currents, low titrated virus concentrations, or low survival times following the injection. For more information on experimental troubleshooting, see Table 2 of Harris et al. (2012).

Finally, our manual QC identified n=11 injections with cortical leakage, a failure mode likely caused by the passage of a leaking needle through the cortex when injecting deep, subcortical regions. Previous versions of the homogeneous and RVM assigned the projections from these experiments to both the primary and the secondary injection sites, or assigned the projection to the centroid of the overall injection volume (Oh et al., 2014; Knox et al., 2018). However, due to the difficulty in disentangling which projections were connected to the primary versus secondary

injection site, and since the injection centroid's location was biased by the off-target cortical injection volume, we chose to remove these experiments.

After our QC, we rebuilt the homogeneous and RVMs, keeping all algorithmic parameters the same but removing the n=56 failed experiments. Notably, in both models, we observed strong continuous losses and gains in connectivity aggregated across major brain divisions, with stronger losses and gains in contralateral than ipsilateral connectivity (Figure 4). The losses in contralateral connectivity are likely due to the n=4 experiments that were removed due to nonspecific tracer spreading, whereas the gains in connectivity are due to removal of n=11 experiments with small amounts of tracer spreading from the injection site, which could have originally diluted contralateral connectivity to a given brain region.

We interpreted our post-QC percentile changes (Supplementary Figures 5A and 6A) as losses in spurious connectivity and gains in meaningful connectivity. Follow-up analyses, solely examining the top 20% of connection strengths in the old versus new connectomes, revealed losses in cerebellum-isocortex and hippocampus-medulla connections in both models. To our knowledge, previous tractography studies in mice do not show monosynaptic connections between the cerebellum and isocortex (Schröder et al., 2020; Kang et al., 2021) or between the hippocampus and medulla (Schröder et al., 2020; Cembrowski et al., 2018; Qiu et al., 2024); therefore, we view these connections as implausible. As a result of downweighting these implausible connections, in both models, we also observed gains in previously-characterized hypothalamus-isocortex (Jiao et al., 2025; Risold et al., 1997) connectivity specifically in the lateral zone of the hypothalamus, hypothalamus-cerebellum connectivity (Onat and Çavdar 2003; Zhu et al., 2006; Dietrichs 1984), and midbrain-cerebellum connectivity, including connections between two raphe nuclei and the paraflocculus of the cerebellum in the RVM (Oostland and Hooft 2016; Waterhouse et al., 1986), further confirming our approach. When examining the top 5% of connections, the 100% loss in hippocampus-medulla connections in the RVM persisted; however, the other changes in connectivity only existed at the 20% threshold, underscoring the need to explore which connectomic changes persist across a variety of connectome density thresholds.

Despite these consistencies, we also observed differences in the changes in both connectomes after QC due to the inherent algorithmic differences between the regionalized voxel and HMs. Some striking examples include a 100% loss in the top 20% of connections between the olfactory bulb and ipsilateral medulla in the RVM (Supplementary Figure 5B) but a 100% gain in the HM (Supplementary Figure 6B), as well as a 100% loss in contralateral striatum-medulla connections in the RVM, but a 500% gain in the HM. To ensure robustness to missing data, we suggest using the RVM over the HM, since the algorithm from Knox et al.(2018) estimates voxel-level connectivity using a distance-weighted average of connectivity within broad major brain divisions, rather than assigning the connectivity from a given experiment to only the brain regions immediately injected. Indeed, due to the lack of existing evidence for monosynaptic olfactory bulb-medulla or striatum-medulla connections (Imamura et al., 2020; Schröder et al., 2020; Märtin et al., 2019; Nakano et al., 2000), we posit that the RVM is a more biologically accurate representation of the mouse structural connectome.

Finally, as a vignette to demonstrate architectural changes following QC, we repeated a modified version of the rich club and community detection algorithm with a binarized matrix of the top 20% of connections in the RVM (Figure 5) (Herrera-Portillo et al., 2025; Coletta et al., 2020). Notably, our QC'd, regionalized connectome showed consistencies with previous graph theoretical analyses at the voxel level (Coletta et al., 2020), and our QC process minimally changed the overall rich club regions. Consistent with Coletta et al. (2020), we implicate the nucleus reuniens of the thalamus as a rich club region, which has been shown to affect cognition in perturbational studies in mice (Vetere et al. 2017). We also showed the emergence of four communities in our structural connectome, with subtle changes in community assignments for n=6 regions after QC. Certain thalamic regions, including the lateral habenula, switched assignments from cortical to brainstem/hippocampus communities, consistent with previous tracer experiments showing direct habenula-cerebellum and anteromedial nucleus-hippocampal connections (Huang et al., 2024; de Lima et al., 2017). On the other hand, the preparasubthalamic and parasubthalamic nuclei, as well as the substantia nigra, switched from the midbrain to the cortex/olfactory community, in line with evidence of cortical connections from other tracer experiments (Goto and Swanson, 2004; Casello and Carter, 2026). Finally, prior work in mice has implicated a circuit connecting the olfactory bulb, amygdala, and hippocampus, which is recapitulated in our changed community assignment for the central amygdalar region to the cortex/olfactory community after QC (Cadiz-Moretti et al., 2016; Schröder et al., 2020). Nonetheless, this community reorganization differs after normalizing connection strengths by region size (Supplementary Figure 9B) (i.e. normalized connection density), necessitating further analysis using isotropic voxels, or equally-sized parcellations. We also note that the rich club and community metrics are biased by the most highly connected brain regions, which did not change after QC. We encourage future work to explore the effects of our QC'd connectomes on metrics that are more sensitive to connectomic changes; for example, the "average shortest path" metric is biased by adding a single false positive or false negative connection, resulting in many nodes with significantly shortened paths (Kitsak et al., 2023)

Although we interpret our rebuilt connectomes as more biologically plausible than the existing connectomes, our work has several limitations. Firstly, our QC depends on binary thresholding. We justified this choice based on the exclusion of noisy background fluorescence, but our thresholding choice could also artificially exclude meaningful connections. Nonetheless, one of our raters (V.N.) repeated the manual QC for all injection and projection data at a lower (0.01) threshold and saw similar results (Supplementary Data 1), suggesting that our failures were not threshold-dependent. Additionally, we did not change the algorithms underlying the RVM or HM to accommodate for the lower number of included experiments, which could result in the overfitting of connectivity to certain brain regions with large losses in injection experiments, such as the cerebellar or hypothalamic regions with a complete loss in injection experiments (Figure 3B). Thirdly, we cannot exclude the possibility that experiments with the smallest projection volumes, especially in the cerebellum, meaningfully represent short-range connectivity to smaller axons, such as cerebellar Purkinje cell axons (Perge et al., 2012); however, due to their small volumes, these experiments have limited utility in whole-brain contexts like MRI-based analyses (Yee et al., 2018), and are similar to previously-excluded experiments in Knox et al. (2018), confirming our decision to exclude them. Finally, for experiments with off-target injections, we discarded the entire experiment, resulting in a loss in connectivity. However, a more sophisticated approach could disentangle the connectivity to

voxels in the intended target injection region, resulting in the inclusion of more experimental data.

The AMBCA is the product of an immense scientific effort by the Allen Institute, and has been incredibly valuable to the neuroscientific community. To further improve its use in light of our findings, we encourage the community to use our rebuilt connectomes, leveraging the data within a subset of the AMBCA to produce more reliable estimates of structural connectivity in the mouse brain. We also have provided evidence for the fact that our rebuilt connectomes subtly alter downstream analyses applying whole-brain structural connectivity, including the characterization of rich clubs and communities at the regional level. We anticipate that our QC'd connectomes will have downstream impacts on a wide variety of mechanistic and pathological models using the original connectomes (Tullo et al., 2025; Rahayel et al., 2022; Henderson et al., 2019; Lubben et al., 2024). Moreover, since the AMBCA experiments were used to build the CCFv3 template, future work needs to assess the effects of excluding misaligned experiments on the anatomy of this commonly-used template. Finally, we hope that future work will extend the application of our QC criteria to the entire AMBCA, consisting of n=2,995 experiments in C57BL/6 mice and other transgenic mouse lines that visualize specific cell types of interest.

**References**


Ashourvan, A., Telesford, Q. K., Verstynen, T., Vettel, J. M., & Bassett, D. S. (2019). Multi-scale detection of hierarchical community architecture in structural and functional brain networks. *PloS One*, *14*(5), e0215520.

Behrens, T. E. J., & Sporns, O. (2012). Human connectomics. *Current Opinion in Neurobiology*, *22*(1), 144–153.

Brooks, S. J., Jones, V. O., Wang, H., Deng, C., Golding, S. G. H., Lim, J., Gao, J., Daoutidis, P., & Stamoulis, C. (2024). Community detection in the human connectome: Method types, differences and their impact on inference. *Human Brain Mapping*, *45*(5), e26669.

Casello, S. M., & Carter, A. G. (2026). Substantia nigra pars reticulata regulates prefrontal cortex via ventromedial thalamus. In *bioRxiv*. bioRxiv. https://doi.org/10.64898/2026.01.13.699372

Cembrowski, M. S., Phillips, M. G., DiLisio, S. F., Shields, B. C., Winnubst, J., Chandrashekar, J., Bas, E., & Spruston, N. (2018). Dissociable structural and functional hippocampal outputs via distinct subiculum cell classes. *Cell*, *173*(5), 1280-1292.e18.

Coletta, L., Pagani, M., Whitesell, J. D., Harris, J. A., Bernhardt, B., & Gozzi, A. (2020). Network structure of the mouse brain connectome with voxel resolution. *Science Advances*, *6*(51), eabb7187.

Cornblath, E. J., Li, H. L., Changolkar, L., Zhang, B., Brown, H. J., Gathagan, R. J., Olufemi, M. F., Trojanowski, J. Q., Bassett, D. S., Lee, V. M. Y., & Henderson, M. X. (2021). Computational modeling of tau pathology spread reveals patterns of regional vulnerability and the impact of a genetic risk factor. *Science Advances*, *7*(24), eabg6677.

de Lima, M. A. X., Baldo, M. V. C., & Canteras, N. S. (2017). A role for the anteromedial thalamic nucleus in the acquisition of contextual fear memory to predatory threats. *Brain Structure & Function*, *222*(1), 113–129.

Desrosiers-Grégoire, G., Devenyi, G. A., Grandjean, J., & Chakravarty, M. M. (2024). A standardized image processing and data quality platform for rodent fMRI. *Nature Communications*, *15*(1), 6708.

Dietrichs, E. (1984). Cerebellar autonomic function: direct hypothalamocerebellar pathway. *Science (New York, N.Y.)*, *223*(4636), 591–593.

Dorr, A. E., Lerch, J. P., Spring, S., Kabani, N., & Henkelman, R. M. (2008). High resolution three-dimensional brain atlas using an average magnetic resonance image of 40 adult C57Bl/6J mice. *NeuroImage*, *42*(1), 60–69.

Feng, D., Lau, C., Ng, L., Li, Y., Kuan, L., Sunkin, S. M., Dang, C., & Hawrylycz, M. (2015). Exploration and visualization of connectivity in the adult mouse brain. *Methods (San Diego, Calif.)*, *73*, 90–97.

Fornito, A., Zalesky, A., & Breakspear, M. (2013). Graph analysis of the human connectome: promise, progress, and pitfalls. *NeuroImage*, *80*, 426–444.

Germann, J., Gouveia, F. V., Chakravarty, M. M., & Devenyi, G. A. (2025). Longitudinal deformation-based morphometry pipeline to study neuroanatomical differences in structural MRI based on SyN unbiased templates. *Aperture Neuro*, *5*. https://doi.org/10.52294/001c.133510

Gollo, L. L., Zalesky, A., Hutchison, R. M., van den Heuvel, M., & Breakspear, M. (2015). Dwelling quietly in the rich club: brain network determinants of slow cortical fluctuations. *Philosophical Transactions of the Royal Society of London. Series B, Biological Sciences*, *370*(1668), 20140165.

Goto, M., & Swanson, L. W. (2004). Axonal projections from the parasubthalamic nucleus. *The Journal of Comparative Neurology*, *469*(4), 581–607.

Harris, J. A., Mihalas, S., Hirokawa, K. E., Whitesell, J. D., Choi, H., Bernard, A., Bohn, P., Caldejon, S., Casal, L., Cho, A., Feiner, A., Feng, D., Gaudreault, N., Gerfen, C. R., Graddis, N., Groblewski, P. A., Henry, A. M., Ho, A., Howard, R., … Zeng, H. (2019). Hierarchical organization of cortical and thalamic connectivity. *Nature*, *575*(7781), 195–202.

Harris, J. A., Oh, S. W., & Zeng, H. (2012). Adeno-associated viral vectors for anterograde axonal tracing with fluorescent proteins in nontransgenic and cre driver mice. *Current Protocols in Neuroscience*, *Chapter 1*(1), Unit 1.20.1-18.

Henderson, M. X., Cornblath, E. J., Darwich, A., Zhang, B., Brown, H., Gathagan, R. J., Sandler, R. M., Bassett, D. S., Trojanowski, J. Q., & Lee, V. M. Y. (2019). Spread of α-synuclein pathology through the brain connectome is modulated by selective vulnerability and predicted by network analysis. *Nature Neuroscience*, *22*(8), 1248–1257.

Herrera Portillo, L., Gallino, D., Yee, Y., Muir, J., Devenyi, G. A., Bagot, R. C., & Chakravarty, M. (2025). Whole brain dimensional approach identifies shared and sex-specific networks of stress susceptibility in male and female mice. In *bioRxiv*. https://doi.org/10.1101/2025.05.10.653278

Huang, H., Liu, X., Wang, L., & Wang, F. (2024). Whole-brain connections of glutamatergic neurons in the mouse lateral habenula in both sexes. *Biology of Sex Differences*, *15*(1), 37.

Hubert, M., & Vandervieren, E. (2008). An adjusted boxplot for skewed distributions. *Computational Statistics & Data Analysis*, *52*(12), 5186–5201.

Imamura, F., Ito, A., & LaFever, B. J. (2020). Subpopulations of projection neurons in the olfactory bulb. *Frontiers in Neural Circuits*, *14*, 561822.

Ioanas, H.-I., Marks, M., Zerbi, V., Yanik, M. F., & Rudin, M. (2021). An optimized registration workflow and standard geometric space for small animal brain imaging. *NeuroImage*, *241*(118386), 118386.

Jiao, Z., Gao, T., Wang, X., Wang, A., Ma, Y., Feng, L., Gao, L., Gou, L., Zhang, W., Biglari, N., Boxer, E. E., Steuernagel, L., Ding, X., Yu, Z., Li, M., Gao, M., Hao, M., Zhou, H., Cao, X., … Xu, X. (2025). Projectome-based characterization of hypothalamic peptidergic neurons in male mice. *Nature Neuroscience*, *28*(5), 1073–1088.

Kang, S., Jun, S., Baek, S. J., Park, H., Yamamoto, Y., & Tanaka-Yamamoto, K. (2021). Recent advances in the understanding of specific efferent pathways emerging from the cerebellum. *Frontiers in Neuroanatomy*, *15*, 759948.

Kebschull, J. M., Richman, E. B., Ringach, N., Friedmann, D., Albarran, E., Kolluru, S. S., Jones, R. C., Allen, W. E., Wang, Y., Cho, S. W., Zhou, H., Ding, J. B., Chang, H. Y., Deisseroth, K., Quake, S. R., & Luo, L. (2020). Cerebellar nuclei evolved by repeatedly duplicating a conserved cell-type set. *Science (New York, N.Y.)*, *370*(6523). https://doi.org/10.1126/science.abd5059

Kitsak, M., Ganin, A., Elmokashfi, A., Cui, H., Eisenberg, D. A., Alderson, D. L., Korkin, D., & Linkov, I. (2023). Finding shortest and nearly shortest path nodes in large substantially incomplete networks by hyperbolic mapping. *Nature Communications*, *14*(1), 186.

Knox, J. E., Harris, K. D., Graddis, N., Whitesell, J. D., Zeng, H., Harris, J. A., Shea-Brown, E., & Mihalas, S. (2019). High-resolution data-driven model of the mouse connectome. *Network Neuroscience (Cambridge, Mass.)*, *3*(1), 217–236.

Kuan, L., Li, Y., Lau, C., Feng, D., Bernard, A., Sunkin, S. M., Zeng, H., Dang, C., Hawrylycz, M., & Ng, L. (2015). Neuroinformatics of the Allen Mouse Brain Connectivity Atlas. *Methods (San Diego, Calif.)*, *73*, 4–17.

Lubben, N., Brynildsen, J. K., Webb, C. M., Li, H. L., Leyns, C. E. G., Changolkar, L., Zhang, B., Meymand, E. S., O'Reilly, M., Madaj, Z., DeWeerd, D., Fell, M. J., Lee, V. M. Y., Bassett, D. S., & Henderson, M. X. (2024). LRRK2 kinase inhibition reverses G2019S mutation-dependent effects on tau pathology progression. *Translational Neurodegeneration*, *13*(1), 13.

Maechler, M., Rousseeuw, P., Croux, C., Todorov, V., Salibian-Barrera, M., Verbeke, T., Koller, M., Conceicao, E. L., & Di Palma, A. (2025). *robustbase: Basic Robust Statistics. R package version 0*. 99–105.

Märtin, A., Calvigioni, D., Tzortzi, O., Fuzik, J., Wärnberg, E., & Meletis, K. (2019). A spatiomolecular map of the striatum. *Cell Reports*, *29*(13), 4320-4333.e5.

Mezias, Chris, LoCastro, E., Xia, C., & Raj, A. (2017). Connectivity, not region-intrinsic properties, predicts regional vulnerability to progressive tau pathology in mouse models of disease. *Acta Neuropathologica Communications*, *5*(1), 61.

Mezias, Christopher, Rey, N., Brundin, P., & Raj, A. (2020). Neural connectivity predicts spreading of alpha-synuclein pathology in fibril-injected mouse models: Involvement of retrograde and anterograde axonal propagation. *Neurobiology of Disease*, *134*(104623), 104623.

Nakano, K., Kayahara, T., Tsutsumi, T., & Ushiro, H. (2000). Neural circuits and functional organization of the striatum. *Journal of Neurology*, *247 Suppl 5*, V1-15.

Oh, S. W., Harris, J. A., Ng, L., Winslow, B., Cain, N., Mihalas, S., Wang, Q., Lau, C., Kuan, L., Henry, A. M., Mortrud, M. T., Ouellette, B., Nguyen, T. N., Sorensen, S. A., Slaughterbeck, C. R., Wakeman, W., Li, Y., Feng, D., Ho, A., … Zeng, H. (2014). A mesoscale connectome of the mouse brain. *Nature*, *508*(7495), 207–214.

Onat, F., & Cavdar, S. (2003). Cerebellar connections: hypothalamus. *Cerebellum (London, England)*, *2*(4), 263–269.

Oostland, M., & van Hooft, J. A. (2016). Serotonin in the cerebellum. In *Essentials of Cerebellum and Cerebellar Disorders* (pp. 243–247). Springer International Publishing.

Perge, J. A., Niven, J. E., Mugnaini, E., Balasubramanian, V., & Sterling, P. (2012). Why do axons differ in caliber? *The Journal of Neuroscience: The Official Journal of the Society for Neuroscience*, *32*(2), 626–638.

Qiu, L. R., Fernandes, D. J., Szulc-Lerch, K. U., Dazai, J., Nieman, B. J., Turnbull, D. H., Foster, J. A., Palmert, M. R., & Lerch, J. P. (2018). Mouse MRI shows brain areas relatively larger in males emerge before those larger in females. *Nature Communications*, *9*(1), 2615.

Qiu, S., Hu, Y., Huang, Y., Gao, T., Wang, X., Wang, D., Ren, B., Shi, X., Chen, Y., Wang, X., Wang, D., Han, L., Liang, Y., Liu, D., Liu, Q., Deng, L., Chen, Z., Zhan, L., Chen, T., … Xu, C. (2024). Whole-brain spatial organization of hippocampal single-neuron projectomes. *Science (New York, N.Y.)*, *383*(6682), eadj9198.

Rahayel, S., Mišić, B., Zheng, Y.-Q., Liu, Z.-Q., Abdelgawad, A., Abbasi, N., Caputo, A., Zhang, B., Lo, A., Kehm, V., Kozak, M., Yoo, H. S., Dagher, A., & Luk, K. C. (2022). Differentially targeted seeding reveals unique pathological alpha-synuclein propagation patterns. *Brain: A Journal of Neurology*, *145*(5), 1743–1756.

Ramirez, D. M. O., Whitesell, J. D., Bhagwat, N., Thomas, T. L., Ajay, A. D., Nawaby, A., Delatour, B., Bay, S., LaFaye, P., Knox, J. E., Harris, J. A., Meeks, J. P., & Diamond, M. I. (2023). Endogenous pathology in tauopathy mice progresses via brain networks. In *bioRxivorg*. https://doi.org/10.1101/2023.05.23.541792

Richards, K., Watson, C., Buckley, R. F., Kurniawan, N. D., Yang, Z., Keller, M. D., Beare, R., Bartlett, P. F., Egan, G. F., Galloway, G. J., Paxinos, G., Petrou, S., & Reutens, D. C. (2011). Segmentation of the mouse hippocampal formation in magnetic resonance images. *NeuroImage*, *58*(3), 732–740.

Risold, P. Y., Thompson, R. H., & Swanson, L. W. (1997). The structural organization of connections between hypothalamus and cerebral cortex. *Brain Research. Brain Research Reviews*, *24*(2–3), 197–254.

Rubinov, M., Thivierge, J. P., Sporns, O., & Breaskpear, M. (2009). Structural connectivity and nonperiodic synchronization in large-scale networks of spiking neurons. *NeuroImage*, *47*, S147.

Schröder, H., Moser, N., & Huggenberger, S. (2020a). The mouse cerebellum. In *Neuroanatomy of the Mouse* (pp. 153–170). Springer International Publishing.

Schröder, H., Moser, N., & Huggenberger, S. (2020b). The Mouse Hippocampus. In *Neuroanatomy of the Mouse* (pp. 267–288). Springer International Publishing.

Steadman, P. E., Ellegood, J., Szulc, K. U., Turnbull, D. H., Joyner, A. L., Henkelman, R. M., & Lerch, J. P. (2014). Genetic effects on cerebellar structure across mouse models of autism using a magnetic resonance imaging atlas. *Autism Research: Official Journal of the International Society for Autism Research*, *7*(1), 124–137.

Swanson, L. W., Hahn, J. D., & Sporns, O. (2017). Organizing principles for the cerebral cortex network of commissural and association connections. *Proceedings of the National Academy of Sciences of the United States of America*, *114*(45), E9692–E9701.

Thompson, E., Schroder, A., He, T., Shand, C., Soskic, S., Oxtoby, N. P., Barkhof, F., Alexander, D. C., & Alzheimer's Disease Neuroimaging Initiative. (2024). Combining multimodal connectivity information improves modelling of pathology spread in Alzheimer's disease. *Imaging Neuroscience (Cambridge, Mass.)*, *2*, 1–19.

Torok, J., Mezias, C., & Raj, A. (2025). Directionality bias underpins divergent spatiotemporal progression of Alzheimer-related tauopathy in mouse models. *Alzheimer's & Dementia: The Journal of the Alzheimer's Association*, *21*(5), e70092.

Tullo, S., Park, J. S. H., Rahayel, S., Gallino, D., Park, M., Mar, K., Zheng, Y.-Q., del Cid-Pellitero, E., Fon, E. A., Luo, W., Shlaifer, I., Durcan, T. M., Misic, B., Dagher, A., Devenyi, G. A., & Chakravarty, M. M. (2025). In vivo and in silico alpha-synuclein propagation dynamics: The role of genotype, epicentre, and connectivity. In *bioRxiv*. https://doi.org/10.1101/2025.07.18.665565

Ullmann, J. F. P., Watson, C., Janke, A. L., Kurniawan, N. D., & Reutens, D. C. (2013). A segmentation protocol and MRI atlas of the C57BL/6J mouse neocortex. *NeuroImage*, *78*, 196–203.

van den Heuvel, M. P., & Sporns, O. (2011). Rich-club organization of the human connectome. *The Journal of Neuroscience: The Official Journal of the Society for Neuroscience*, *31*(44), 15775–15786.

Wang, Q., Ding, S.-L., Li, Y., Royall, J., Feng, D., Lesnar, P., Graddis, N., Naeemi, M., Facer, B., Ho, A., Dolbeare, T., Blanchard, B., Dee, N., Wakeman, W., Hirokawa, K. E., Szafer, A.,

Sunkin, S. M., Oh, S. W., Bernard, A., … Ng, L. (2020). The Allen Mouse Brain Common Coordinate Framework: A 3D reference atlas. *Cell*, *181*(4), 936-953.e20.

Waterhouse, B. D., Mihailoff, G. A., Baack, J. C., & Woodward, D. J. (1986). Topographical distribution of dorsal and median raphe neurons projecting to motor, sensorimotor, and visual cortical areas in the rat. *The Journal of Comparative Neurology*, *249*(4), 460–476, 478–481.

Yee, Y., Ellegood, J., French, L., & Lerch, J. P. (2024). Organization of thalamocortical structural covariance and a corresponding 3D atlas of the mouse thalamus. *NeuroImage*, *285*(120453), 120453.

Yee, Y., Fernandes, D. J., French, L., Ellegood, J., Cahill, L. S., Vousden, D. A., Spencer Noakes, L., Scholz, J., van Eede, M. C., Nieman, B. J., Sled, J. G., & Lerch, J. P. (2018). Structural covariance of brain region volumes is associated with both structural connectivity and transcriptomic similarity. *NeuroImage*, *179*, 357–372.

Zalesky, A., Fornito, A., Cocchi, L., Gollo, L. L., van den Heuvel, M. P., & Breakspear, M. (2016). Connectome sensitivity or specificity: which is more important? *NeuroImage*, *142*, 407–420.

Zhou, X., Wang, Y., & Si, B. (2025). Controlling epileptic seizures through hippocampal regulation: A complex network analysis in the mouse brain. *IEEE Transactions on Neural Systems and Rehabilitation Engineering*, *33*, 4302–4314.

Zhu, J.-N., Yung, W.-H., Kwok-Chong Chow, B., Chan, Y.-S., & Wang, J.-J. (2006). The cerebellar-hypothalamic circuits: potential pathways underlying cerebellar involvement in somatic-visceral integration. *Brain Research Reviews*, *52*(1), 93–106.

**Supplementary Data:**
https://drive.google.com/drive/folders/17tC8MYei_zRUILBdaghRnujLQXayp29x?usp=sharing

**Data and Code Availability**
All code is stored on https://github.com/vik16nathan/allen_connectome_qc. All data is publicly available and downloaded from the Allen API.

**Author Contributions**
V.N.: Conceptualization, Software, Formal Analysis, Investigation, Writing—Original Draft, Writing—Review & Editing. S.T.: Formal Analysis, Writing—Review & Editing. L.H.: Formal Analysis, Writing—Review & Editing. G.D.: Conceptualization, Writing—Review & Editing. Y.Y.: Conceptualization, Writing—Review & Editing. M.M.C.: Conceptualization, Supervision, Writing—Review & Editing, Funding Acquisition.

**Declaration of Competing Interests**: The authors have no competing interests to declare.

**Funding**
This work was funded by the Fonds de Recherche Quebec, Santé (FRQS), the Canadian Institutes of Health Research (CIHR), the Healthy Brains Healthy Lives (HBHL) initiative, the Translational Initiative in De-Risking Neurotherapeutics (TRIDENT), and the New Frontiers in Research Fund (NFRF).

**Acknowledgements**
We would like to thank Kameron Decker Harris, Jennifer Whitesell, and Stefan Mihalas at the Allen Institute for thoughtful discussions about the tracer data processing involved in building the connectome from Knox et al. (2018). We would also like to thank the authors of Knox et al. (2018), Joseph E. Knox, Kameron Decker Harris, Nile Graddis, Jennifer Whitesell, Hongkui Zeng, Julie A. Harris, Eric Shea-Brown and Stefan Mihalas, for providing the code to recreate the RVM and HM connectomes.

**Supplementary Tables**

**Supplementary Table 1:** List of abbreviations for major division names.

| **Full Major Division Name** | **Major Division Abbreviation** |
|---|---|
| Isocortex | Isocortex |
| Olfactory areas | OLF |
| Hippocampal formation | HPF |
| Cortical sublate | CTXsp |
| Striatum | STR |
| Pallidum | PAL |
| Thalamus | Thal |
| Hypothalamus | Hypothal |
| Midbrain | Midbrain |
| Pons | Pons |
| Medulla | Medulla |
| Cerebellum | CB |

## Supplementary Figures

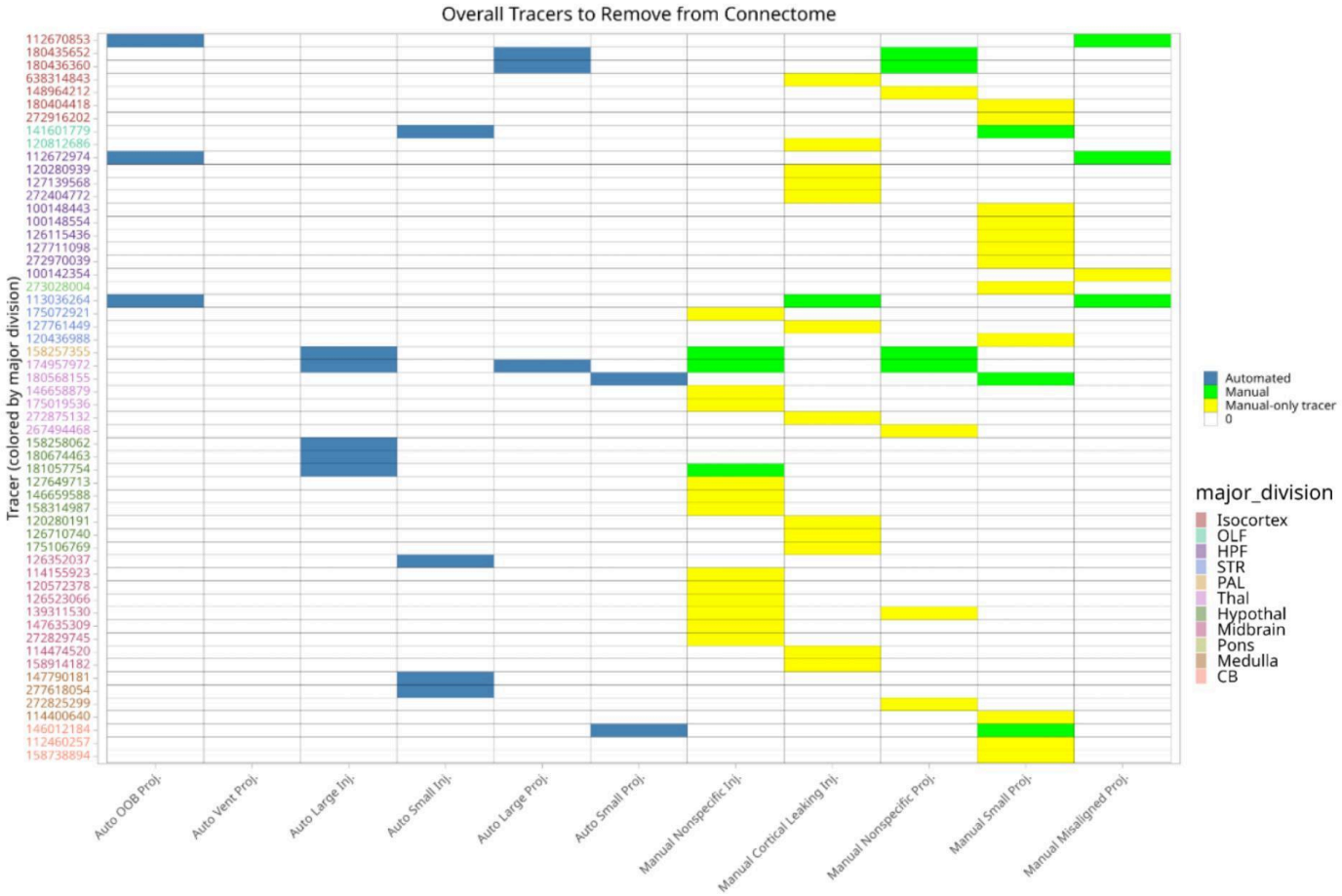


**Supplementary Figure 1:** The complete set of n=56 experiments removed during our QC procedure, organized by the major division of the experimental injection. For each removed experiment, we show the failure mode(s) that result in the experiment's exclusion, differentiating between automated removal criteria in blue and manual removal criteria in yellow/green. If an experiment has a green label for a manual removal criteria, then it was also flagged during automated QC.

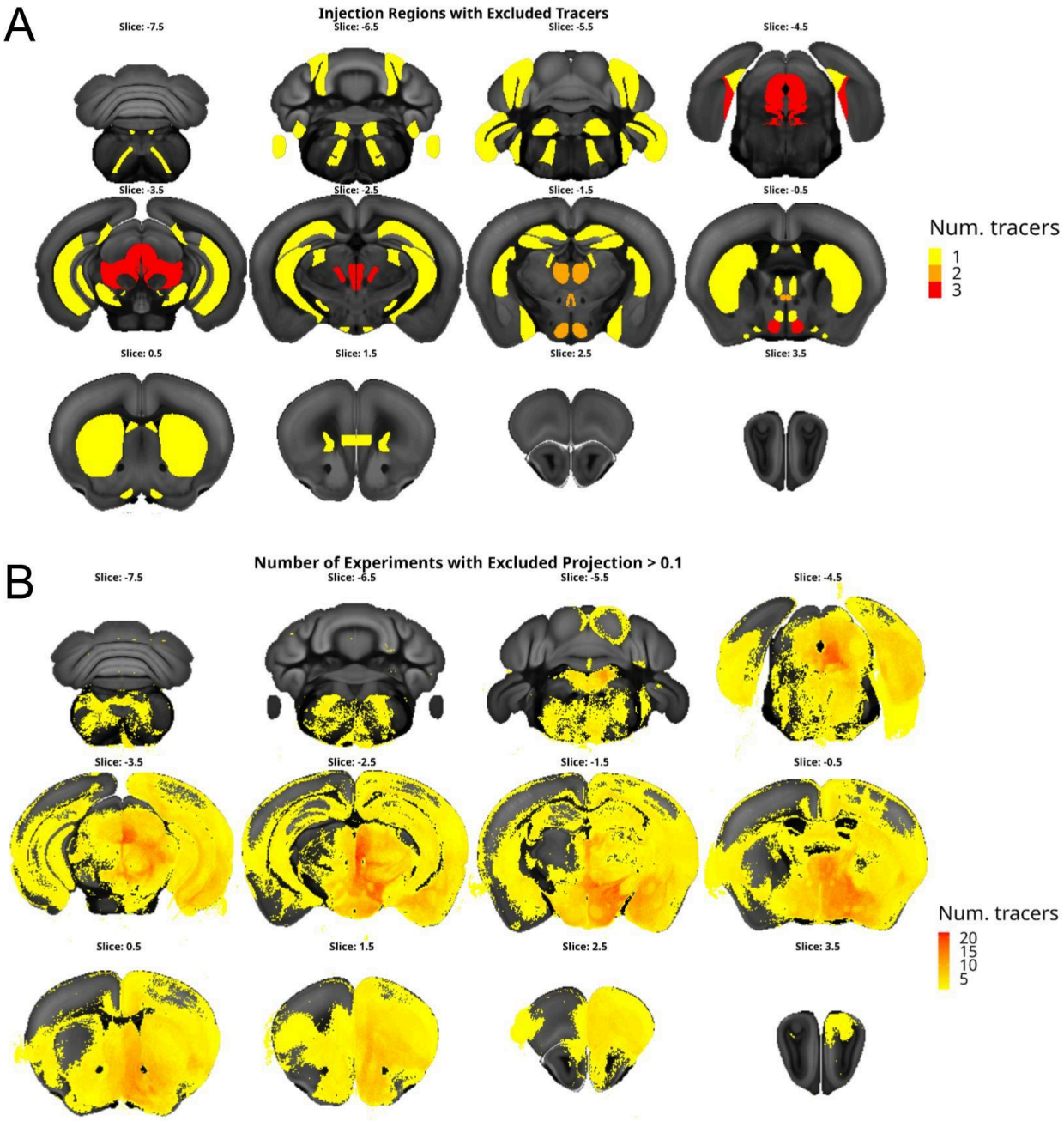


**Supplementary Figure 2:** (A) The number of experimental injections removed from each brain region and (B) the number of experimental projections removed from each voxel, aggregated across all n=56 removed experiments. Note that we chose to show the injections removed per region rather than per voxel due to the relative sparsity of the injection sites compared to the projection data.

A

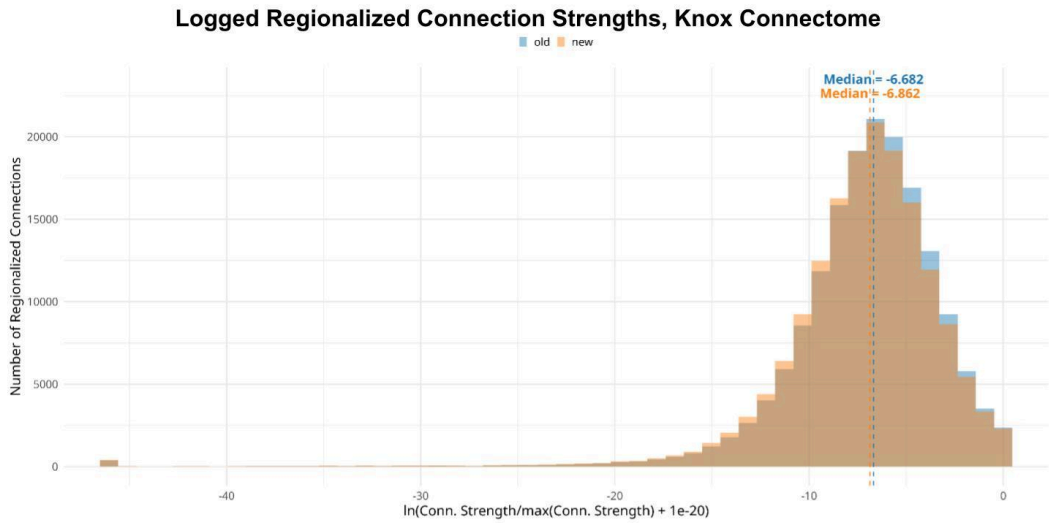


B

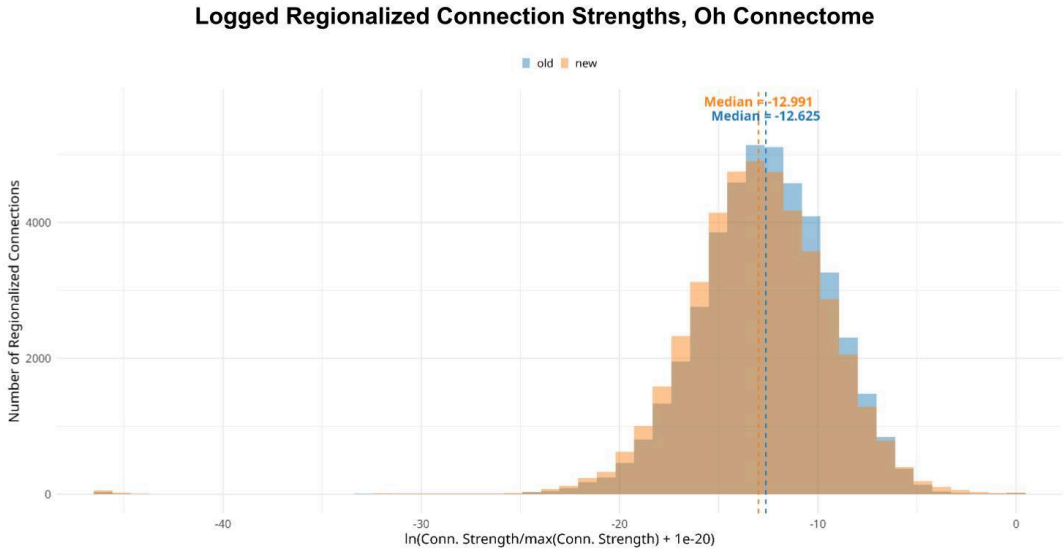


**Supplementary Figure 3:** Histograms showing the distributions of the logged, normalized connection strengths in (A) the RVM and (B) the HM. In each panel, we compare the distribution of the connection strengths before QC (blue) versus after QC (orange).

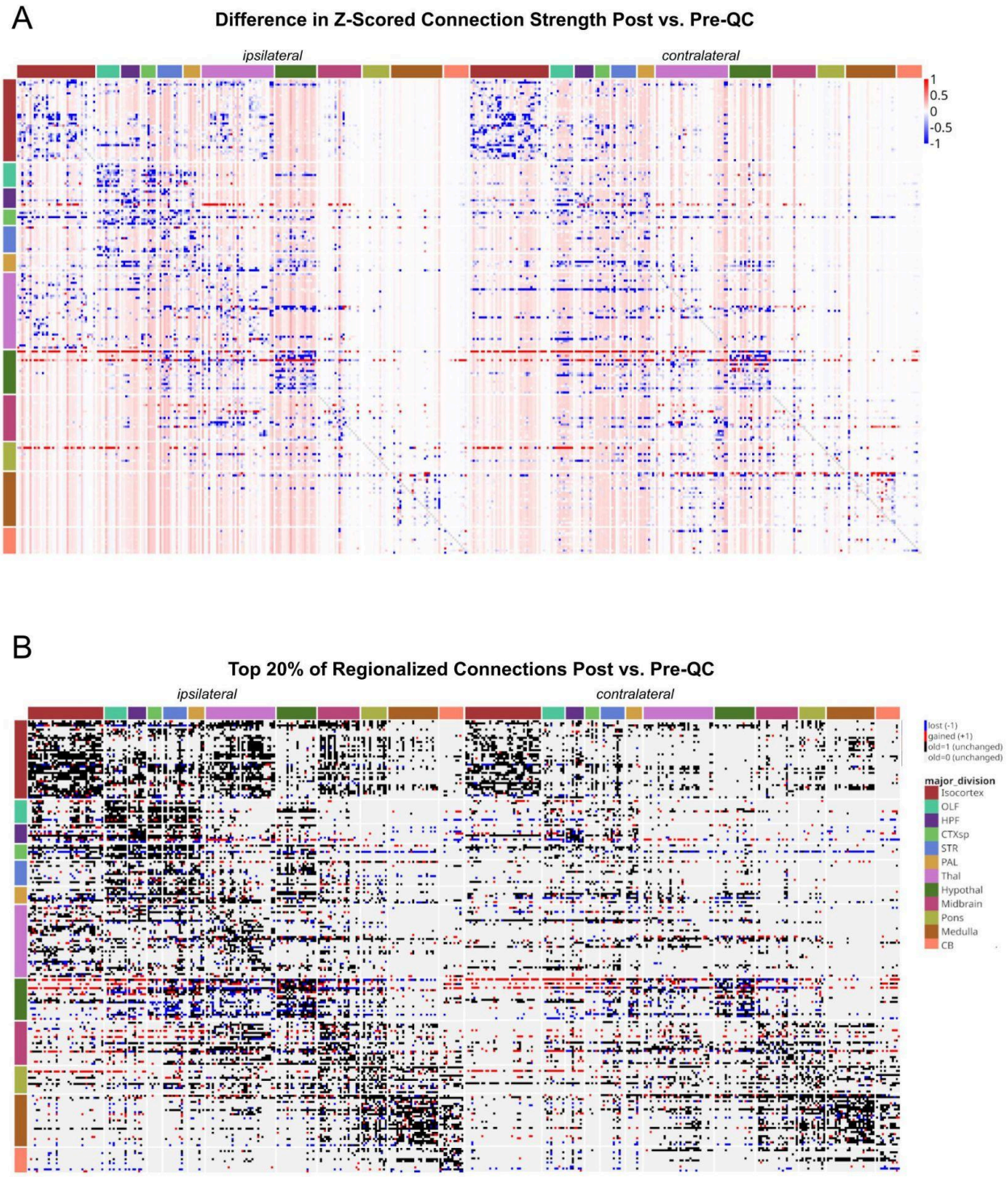


**Supplementary Figure 4:** Similar to Figure 4, we observe whole-brain architectural changes in the HM (n=211 regions) after QC, when examined (A) continuously, when examining the difference in z-scored, normalized connection strengths, thresholded from [-1,1] due to the presence of outliers (B) discretely, when examining the lost (blue), gained (red) and unchanged (black/gray) connections within the subset of the top 20% of the old vs. rebuilt connectomes.

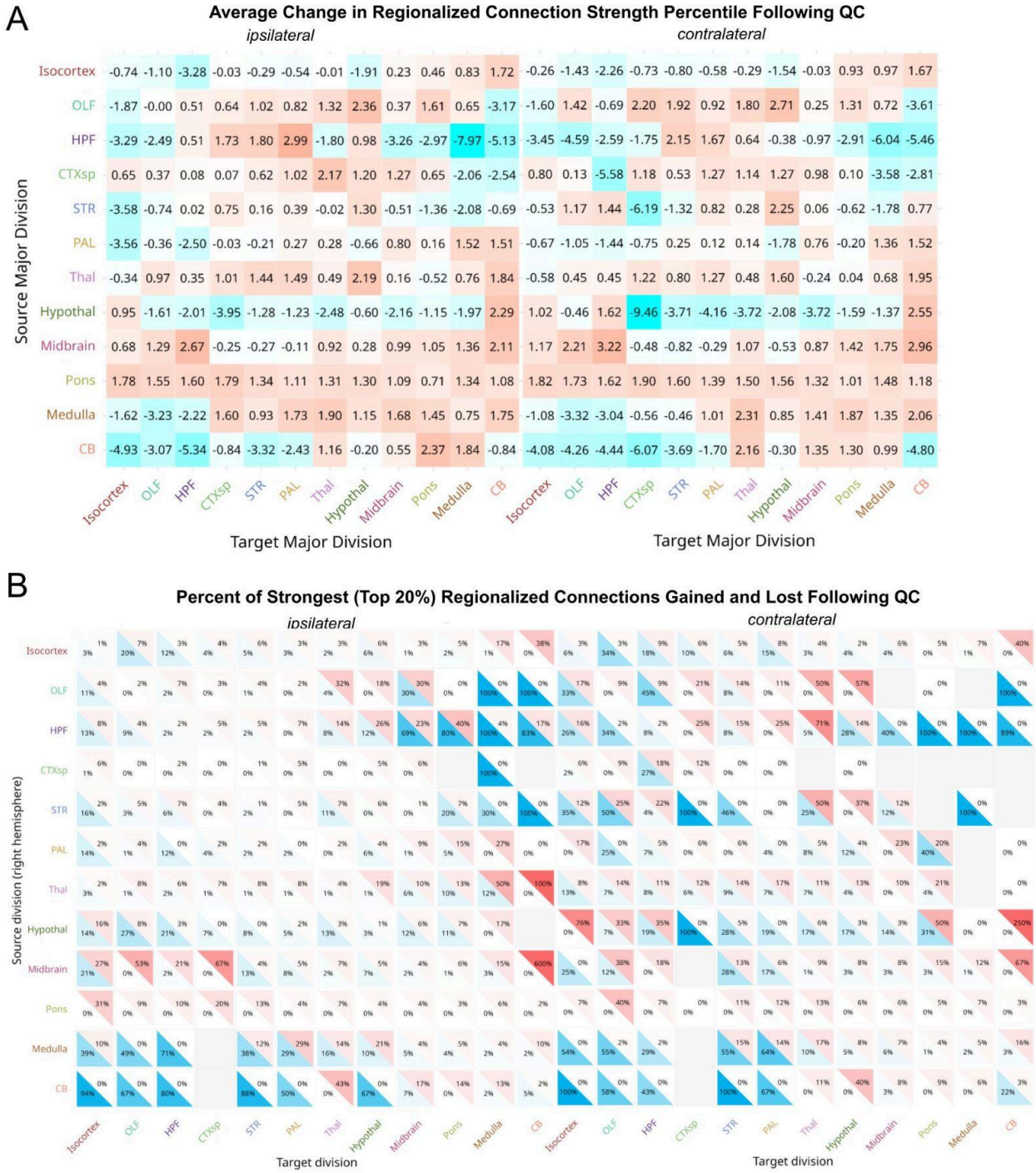


**Supplementary Figure 5:** We aggregate the changes in connectivity from the RVM, showing (A) the average change in connection percentile across all connections and (B) the proportion of the top 20% of connections that were lost or gained, relative to the original number of connections in each major division in the RVM, summarized across each pair of major brain divisions from Knox et al.. For both plots, blue denotes a loss in connectivity and red denotes a gain in connectivity.

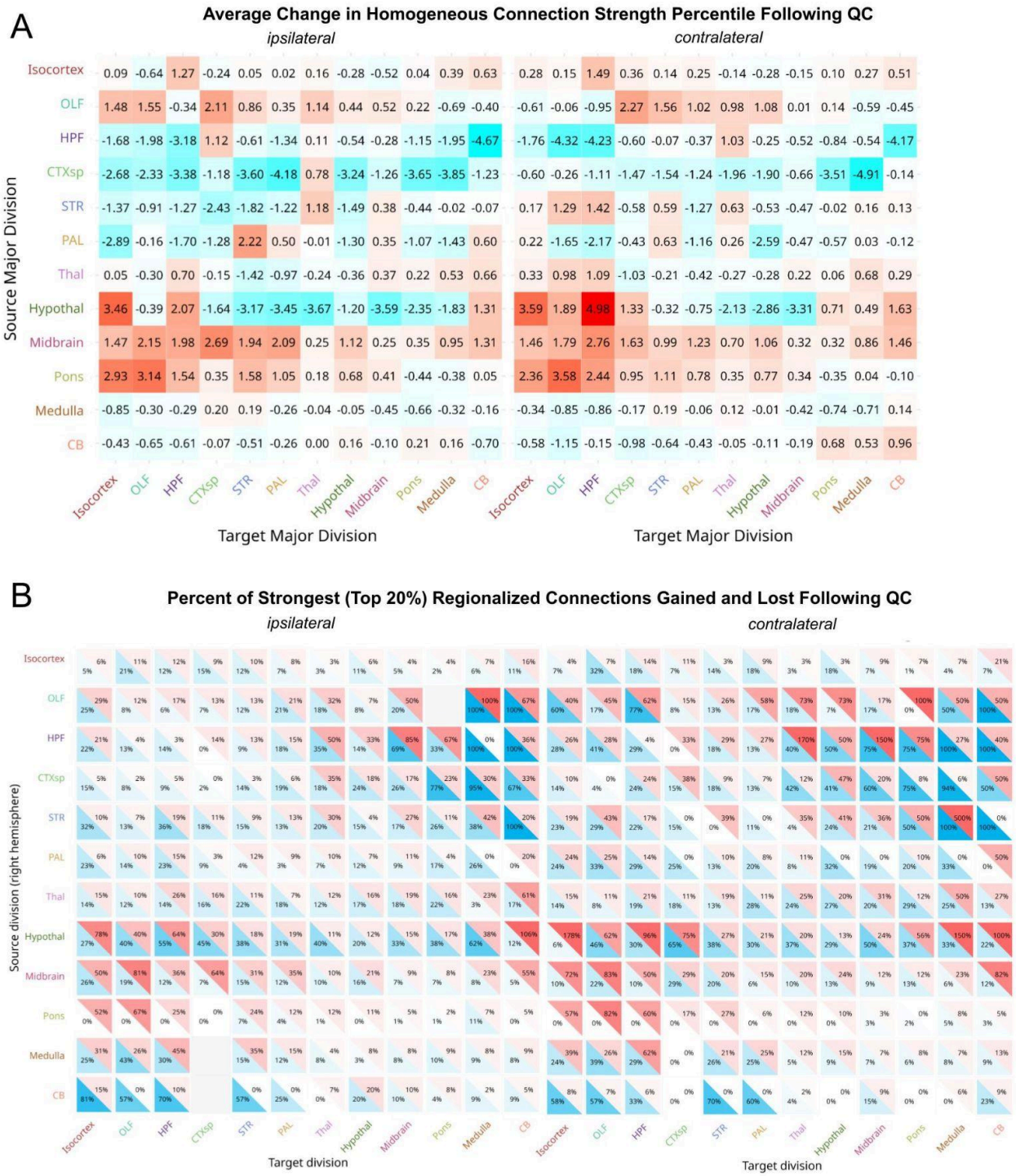


**Supplementary Figure 6:** Similar to Supplementary Figure 5, we aggregate the changes in connectivity from the HM, showing (A) the average change in connection percentile across all connections and (B) the proportion of the top 20% of connections that were lost or gained, summarized across each pair of major brain divisions from Oh et al.. For both plots, blue denotes a loss in connectivity and red denotes a gain in connectivity.

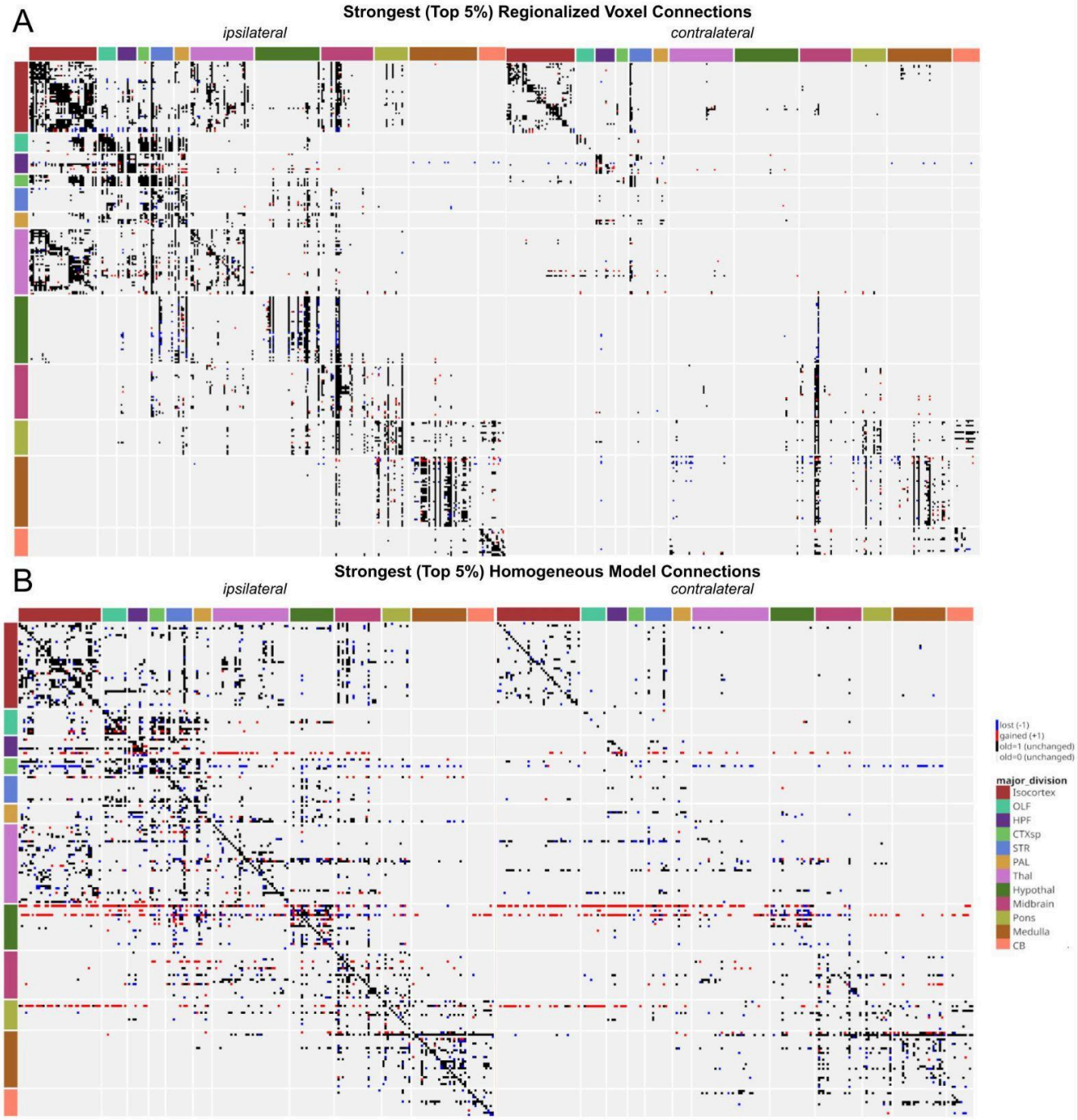


**Supplementary Figure 7:** Similar to Figure 4B, we observe discrete connectivity changes when examining the top 5% of connection strengths in the old vs. rebuilt connectomes. We show lost (blue), gained (red) and unchanged (black/gray) connections within the (A) RVM (B) HM.

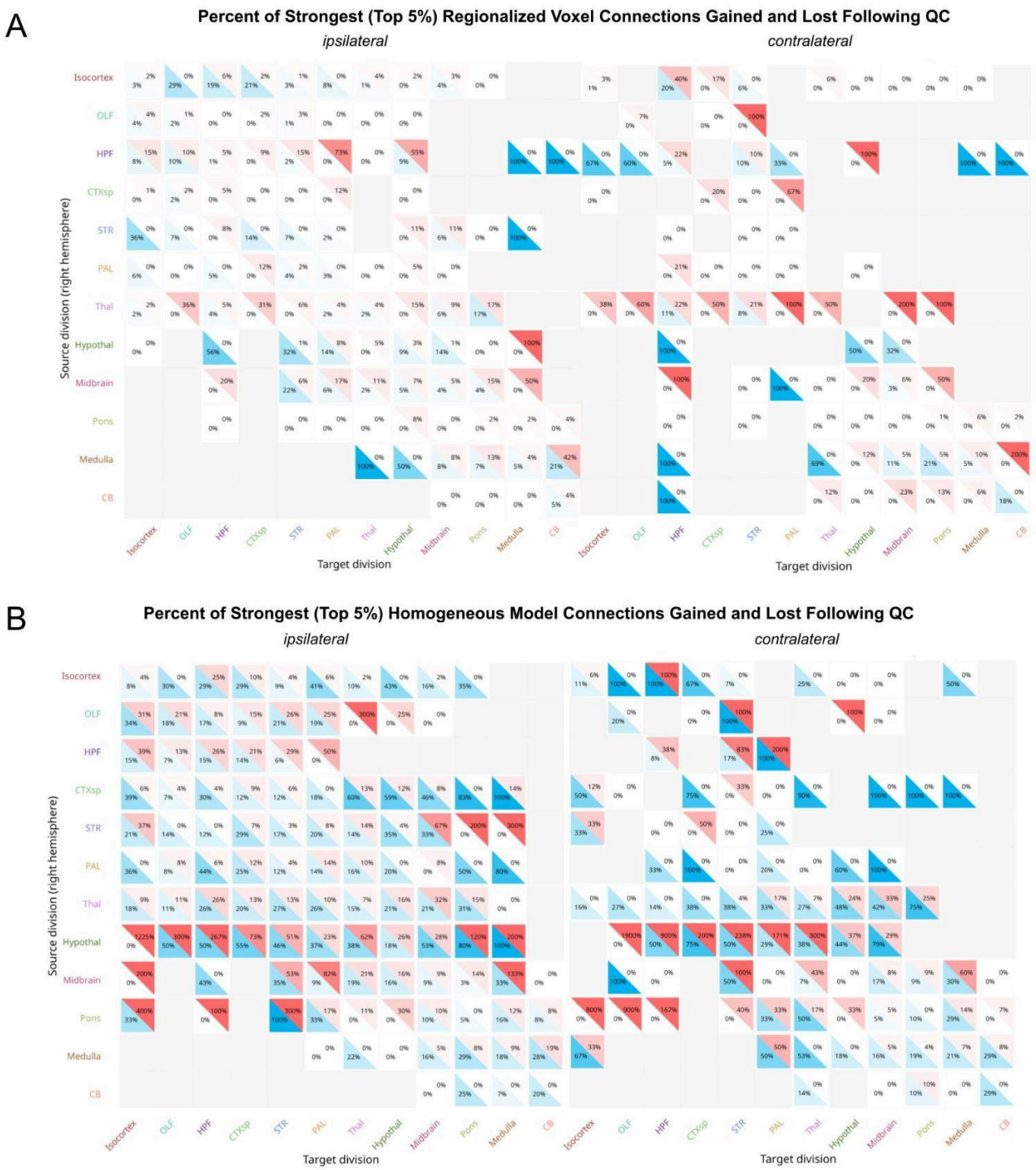


**Supplementary Figure 8:** Similar to Supplementary Figure 5B, we show the proportion of the top 5% of connections that were lost or gained, summarized across each pair of major brain divisions in (A) the RVM and (B) the HM.

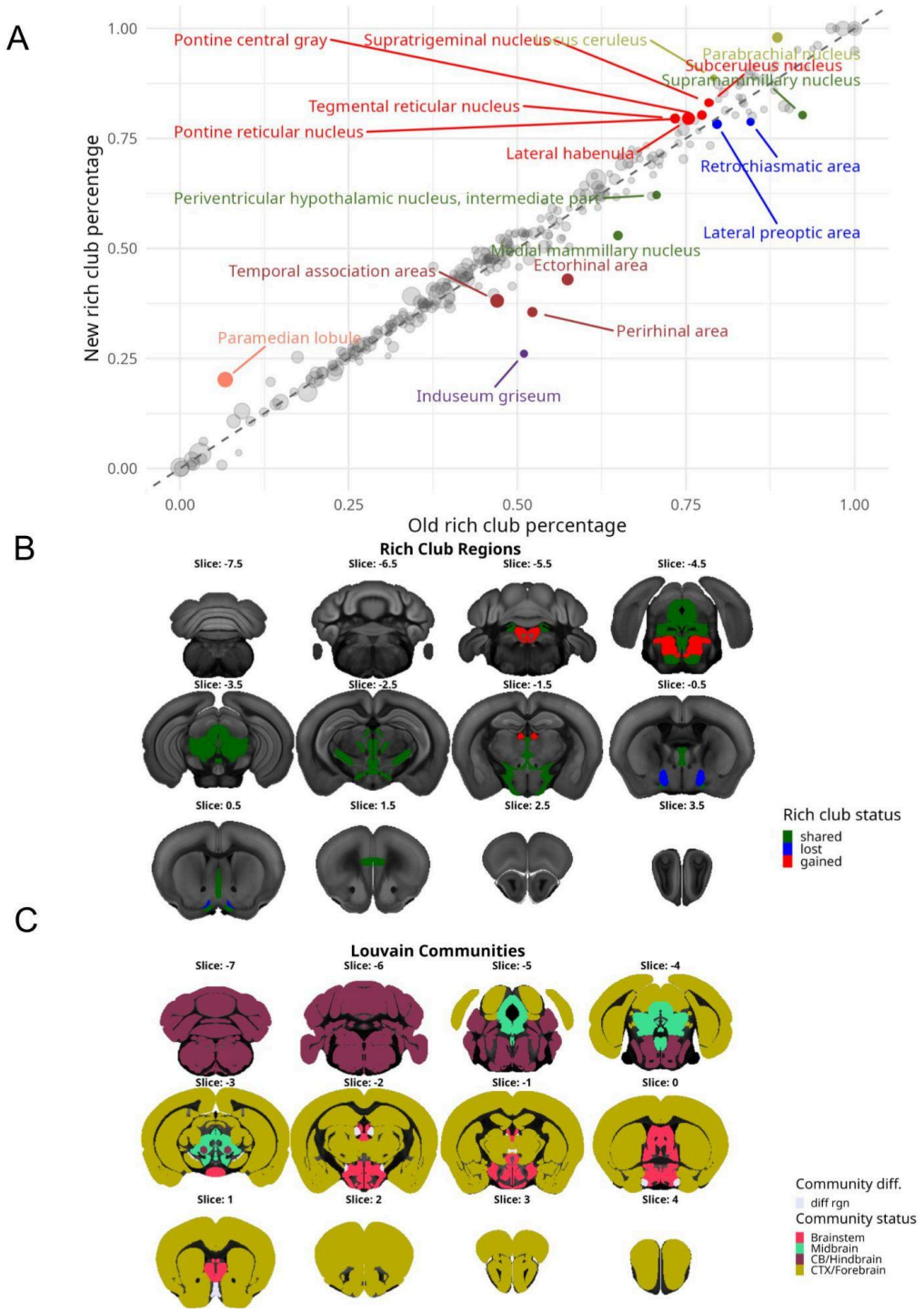


**Supplementary Figure 9:** Similar to Figure 5, we show organizational changes within the top 20% of connections, using the "normalized connection density" instead of the normalized connection strength in the RVM. We assume symmetric connections across hemispheres and see changes in (A) the rich club coefficient, defined as the proportion of "rich" degrees that a given region's degree is greater than or equal to (B) whether a region is "rich" or not, using a threshold of the mean plus one standard deviation of the "rich" degrees, and (C) the Louvain community assignments for each region.

**Supplementary Methods**

*Experimental and 2D Image Processing for Serial Two-Photon Microscopy Data*
To measure connectivity to various brain regions, the Allen Institute used iontophoresis to inject a tracer into the cell bodies of various brain regions in wild-type C57BL/6J mice at P56 ± 2 postnatal days. This recombinant adeno-associated viral (rAAV) tracer expresses enhanced green fluorescent protein (EGFP) under the control of a human synapsin I promoter, thus specifically labelling neurons (Harris et al., 2012). The rAAV tracer anterogradely labels axons without crossing synapses; thus, each experiment represents directed, monosynaptic connections to the injection site. The mice were euthanized 21 days following injection before serial two-photon microscopy at a coronal slice interval of 100 µm and within-slice image resolution of 0.35 µm (Oh et al., 2014).

The scanned two-photon microscopy images were then processed by the Allen Institute. For each experiment, the 2D microscopy images first underwent intensity correction and stitching. The 2D images were then manually quality controlled (QC'd) for specimen and image quality, resulting in the removal of entire experiments with "severe artefacts" (missing tissue, low signal strength, etc.) or the masking of regions with high intensity/frequency artifacts and signal dropout (see Oh et al., 2014). Note that these QC criteria of the 2D images are completely separate from our QC criteria for the 3D images. After these corrections, the projection pixels in each image were identified by a segmentation algorithm that separated fluorescence from background noise (see Kuan et al., 2015 for more details). After segmentation, the injection site(s) were defined manually in each image by drawing closed polygons around the cell bodies of the infected neurons.

*Rich Club Algorithm*

1. Use *rich_club_bd.m* to calculate the rich club coefficient at each degree.
2. Generate 1000 rewired randomized networks using randmio_dir.m; calculate the rich club coefficient at each degree.
3. For each degree, see the proportion of networks from (2) that have a higher rich club coefficient than the coefficients from (1); use this to define which degrees have a significant number of nodes in a rich club
4. Identify a coefficient defining the "topological rich club" (i.e. whether a node is "rich" or not). This is equal to the mean plus one standard deviation of the degrees with significant rich clubs.
    a. Take all the nodes with degrees above this to be "rich club" nodes.
5. For each node with degree $k_n$, calculate the percentage of significant degrees that $k_n$ is greater than or equal to. This is the rich club percentage, to be visualized in Fig. 5. You can now merge contralateral/ipsilateral nodes, since they will have the same rich club percentage.

*Community Detection Algorithm*

1. For each resolution parameter "gamma" from 0.3 to 3, in increments of 0.05:
    a. Run the Louvain community detection algorithm (community_louvain.m) 100 times.

    b. Find the node x node agreement matrix between the 100 repetitions (using consensus_und.m).
    c. Calculate the consensus community assignments from the agreement matrix by using threshold *tau*. The threshold *tau* used to binarize/cluster the agreement matrix is the mean agreement of the ***permuted*** community assignments from (a) (see Lancichinetti & Fortunato, 2012).
2. Write out the community assignments for each gamma.
3. Calculate a gamma x gamma mutual information matrix between the clusterings.
4. Determine which gamma yields the most stable clustering.
    a. For mutual information thresholds between 0.9-1 in increments of 0.005:
        i. Find the consensus clustering of the gamma x gamma matrix at the given threshold.
    b. Calculate the gamma x gamma agreement matrix across all mutual information thresholds.
    c. Visualize all values of this matrix above 0.6; heuristically select gamma in the center of the largest "cluster" of agreement matrix values. We chose gamma=1.3, as this was in the middle of a large “cluster” of agreement matrix values in the old and new regionalized voxel connectomes.
5. Run the Louvain clustering with this gamma 100 times; take the consensus clustering as the community assignments for each node.
6. Manually inspect community assignments and ensure that the numbers assigned for each community are consistent across the old versus the new connectomes. If there are two communities that have the same sets of nodes contralaterally vs. ipsilaterally, they can be merged into a single community.